

NANO-SCALE RAMAN THERMOMETRY OF DIAMOND

By

Oliver Conquest

A THESIS SUBMITTED TO MACQUARIE UNIVERSITY
FOR THE DEGREE OF MASTER OF RESEARCH
DEPARTMENT OF PHYSICS
DECEMBER 2017



EXAMINER'S COPY

© Oliver Conquest, 2017.

Typeset in L^AT_EX 2_ε.

Except where acknowledged in the customary manner, the material presented in this thesis is, to the best of my knowledge, original and has not been submitted in whole or part for a degree in any university.

Oliver Conquest

Acknowledgements

I would like to express my sincere appreciation to those who helped make this thesis possible over the past nine months. I would like to thank my principle supervisor Thomas Volz for his guidance, encouragement and motivation throughout the course of this thesis. Throughout my thesis, Thomas encouraged me to keep learning and applying new skills which will no doubt be indispensable for future endeavors. Also to my co-supervisors Carlo Bradac and Mike Heimlich for their support, expertise and networking which helped push the project forward, thank you.

I'd like to express my gratitude to the following people: Lachlan Rogers for his guidance, inspiration, expertise and long hours helping in and out of the lab. Matt Van Breugel for his encouragement, support in and out of the lab, and always being a good office/lab mate. Sarah Kaiser for her encouragement, support and expertise which has been invaluable. Luke Helt who helped me gain an understanding of the quantum theory behind Raman temperature dependences. To the rest of the QMAPPers Guillermo, Jemy, Sarath and Woody, thank you.

I'd like to give a special thanks to Louise Brown and Lucigem who provided the size sorted nanodiamonds making this thesis possible. And another special thanks to Bryan from our industry partner who gave me the opportunity of a two-week placement and provided ongoing expertise and support throughout this thesis.

Thank you Jo Dawson for being a great MRes Advisor, and fellow masters students for all the activities and lakeside Ubar lunch gatherings. A shout out to the 'Boy0s' you know who you are.

Finally, I would like to thank my friends and family who have always encouraged and motivated me.

Abstract

Raman spectroscopy is well established over a broad range of interdisciplinary applications, which include optical imaging, crystallographic probing, spectroscopy and thermometry. The basis of this thesis is Raman thermometry with nanodiamond, i.e. nano-scale diamond crystals, and its application for characterising integrated transistor circuits. Firstly, an extensive review of Raman scattering, spectroscopy, thermometry and diamond properties is developed. Then, attention is focused on the experimental implementation of Raman thermometry with bulk and 250 nm diamond crystals. As an initial experimental step and under well-controlled conditions, the temperature dependence of the Raman line shift and width is characterised. In a second step, a preliminary measurement on a real semiconductor chip is carried out. The results open up a path towards the practical and robust implementation of a nanoscale temperature sensor for device characterisation.

Contents

Acknowledgements	iv
Abstract	v
1 Introduction	1
1.1 Project Scope and Background	2
1.2 Thesis Overview	3
2 Raman Thermometry	5
2.1 Raman Scattering	5
2.1.1 First Order Raman Scattering	6
2.1.2 Raman Scattering Properties	9
2.2 Diamond	11
2.2.1 Properties of Diamond	12
2.2.2 Raman Scattering from Diamond	15
2.3 Raman Thermal Characteristics	18
2.3.1 Line Shift Temperature Dependence	18
2.3.2 Linewidth Temperature Dependence	18
2.3.3 Fluorescence Temperature Dependence	19
2.4 Raman Thermometry with Diamond	20
2.4.1 Bulk Diamond Thermometry	20
2.4.2 Nano-Scale Diamond Thermometry	20

2.5	Alternate Thermometry Methods in Diamond	21
2.5.1	NV-Spin Temperature Sensing	21
2.5.2	SiV Temperature Sensing	23
2.6	Applications to Electronic Devices	23
3	Methodology	25
3.1	Confocal Microscopy	25
3.2	Lab Built Confocal Microscope	27
3.2.1	Resolution and Efficiency of Confocal System	28
3.2.2	Excitation Source	28
3.2.3	APD Photon Detectors and Imaging Counters	28
3.2.4	Translation, Scanning and Thermal stages	29
3.2.5	Monochromator	31
4	Raman Thermometry with Diamond	32
4.1	Bulk Diamond Characterisation	32
4.2	Nanodiamond Characterisation	38
4.3	GaN FET Device Measurment	41
4.3.1	FET setup and Operation	41
5	Outlook	45
	References	47

1

Introduction

Observing the ‘small world’ was an impossible dream of the early Greek atomists, but advances in optics, material science and quantum physics have allowed us to peer into the ‘small world’. Mankind’s ability to develop compact, reliable and nanoscale technology relies on having a view into this ‘small world’. For instance, the transistor went from being the size of a coffee mug to within the size of a DNA strand, developed in parallel with high-resolution micro-machining, optical lithography and imaging techniques, stimulated by the development of the laser. Our pursuit of ever smaller and more powerful technologies relies on our ability to develop methods for probing properties of the nano-world.

1.1 Project Scope and Background

Localized temperature sensing at the nanoscale is of major significance for today's technology, in particular for developing integrated transistor circuits, the fundamental logic components in modern information technologies. The operational reliability and efficiency of these devices is directly related to their ability to efficiently and effectively dissipate heat. The problem of locally monitoring temperature at the nanoscale is usually tackled by utilising optics-based thermometry techniques, such as infra-red (IR) laser spectroscopy, temperature readout via fiber Bragg gratings (FBG) and conventional Raman thermometry. All of these methods are spatially limited by diffraction and/or device dimensions. Recent studies have employed nanomaterials of sub-diffraction limited sizes, which act as thermometers with spatial resolution set by the scale of the nanomaterial itself [1, 2].

Raman spectroscopy is a firmly established method for characterising material properties. It provides information on sample doping, purity, strain, electric and magnetic fields, lattice orientation and thermal properties. The advent of the laser providing coherent monochromatic light has made Raman scattering an attractive spectroscopy technique over a broad range of disciplines, with applications in biology, geology, chemistry and quantum physics [3–6].

Diamond is a unique material with extraordinary thermal, electrical, optical and mechanical properties. Due to its hardness diamond produces strong Raman spectra compared to other materials making it one of the first materials to have its Raman signal characterised. Nanodiamond (ND) probes have received increasing interest in the fields of medicine, thermal sensing, magnetometry and quantum information technology [7–9]. Diamond synthesis by CVD growth has been developed to the point where impurity levels and general crystal quality can be controlled to a high degree. Nanodiamonds can be produced by ball milling of grown diamond films or by controlled detonation of explosives such as TNT.

This thesis investigates the thermal characteristics of the first-order Raman line in bulk and (detonation) nanodiamond material. The parameters of Raman peak position and line width are studied in each case, and contrasted with previous studies. The applicability of nanodiamond Raman thermometry as an alternative for highly spatially resolved temperature measurements of integrated transistor circuits is explored.

The work for this thesis was conducted over a nine-month period. While the initial plan for the thesis was designed to be predominantly experimental in nature, unforeseen technical difficulties in the diamond lab (complete AC failure over months, broken AFM/confocal setup that was not fixed properly by manufacturer) meant a significant delay in the start of the experiments. In order to bridge the delay in experiments, more time was devoted to exploring and understanding the theory behind Raman scattering and thermal Raman sensing. Hence, the background (theory) section in this thesis is somewhat longer than was initially anticipated. About 4 months into the project, with no working AFM/confocal system available, we decided to build a separate confocal setup providing the capability to carry out basic Raman measurements.

The general idea for the project was developed in collaboration with an industry partner and the present thesis is a starting point for an ongoing collaboration in the future. Due to the nature of the research and the highly competitive semiconductor device market, the partner would like to remain undisclosed. During the Masters project, the author of this thesis was given the opportunity to spend two weeks in a placement position at the industry partner, learning about their design and testing processes for integrated semiconductor chips. This greatly helped the understanding of the requirements for our nanoscale Raman thermometers to be applicable and useful.

1.2 Thesis Overview

The subject of this thesis is Raman thermometry with diamond and its practical application to electronic devices.

Chapter 2: Raman Thermometry

This chapter reviews the physics of Raman scattering, the basic concepts behind Raman thermometry and discusses the special properties of diamond as a ‘Raman active’ material. The electronic, optical and thermal properties of diamond are reviewed along with a short discussion of the Nitrogen Vacancy (NV) defect in diamond. The historical context of Raman scattering from diamond is considered along with the dependence of its Raman signal on temperature.

Raman thermometry with diamond is briefly compared to more recent work on temperature sensing with NV spins. Finally, Raman thermometry for device characterisation is discussed.

Chapter 3: Methodology

The methodology chapter introduces the basic concept of confocal microscopy, and describes the home-built confocal microscope used for Raman thermometry, along with the other parts necessary to run the experiment in particular excitation source and detectors. Spatial resolution and detection efficiencies of our setup are briefly discussed.

Chapter 4: Raman Thermometry with Diamond.

The first part of this chapter presents and analyses measured temperature dependencies of Raman line positions and widths for bulk diamond, and for 250 nm nanodiamond material. The second part discusses the first temperature measurements on a Gallium Nitride (GaN) integrated transistor circuit with our nanodiamond Raman thermometer. Feasibility and reliability of the results are discussed.

Chapter 5: Outlook

Based on the results presented in chapter 4 further conclusions are drawn and possible paths for future work outlined.

2

Raman Thermometry

This chapter first discusses theoretical results on first-order Raman processes. It then describes the special material properties of diamond before introducing the Klemens/Raman thermal models and reviewing their early application to Raman characterisation of diamond. Further it briefly introduces some alternative temperature-sensing techniques that make use of specific defect centers in the diamond lattice. Finally, a short review of standard optical thermometry of integrated transistor circuits is given.

2.1 Raman Scattering

Raman scattering dates back as early as 1928 and was first performed by C.V. Raman. Using filtered and focused sunlight. Besides the resonant Rayleigh signal he also detected scattered light at a red-shifted characteristic frequency which clearly depended on the specific liquid/gas

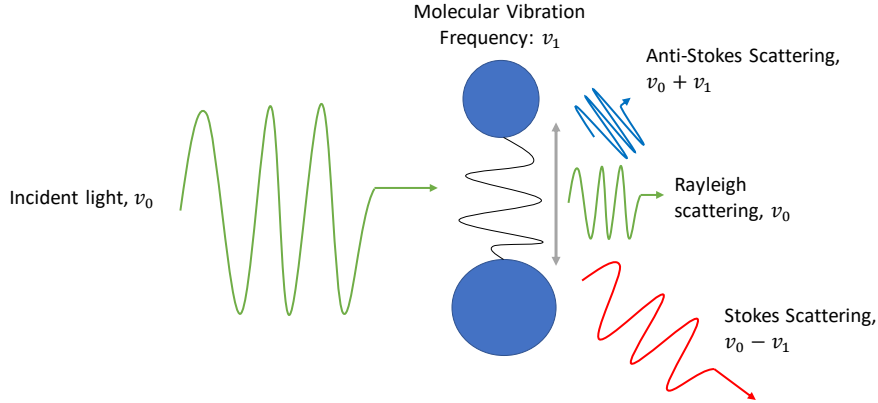


FIGURE 2.1: Basic representation of a diatomic molecule undergoing Raman scattering in the form of the Stokes/Anti-Stokes scattering.

sample. To honor his contribution this form of light scattering became later known as Raman scattering, for which he revied the Nobel prize in 1930 [10].

2.1.1 First Order Raman Scattering

Generally speaking, Raman Scattering is material-dependent inelastic scattering, arising from the modulation of the scatter's response to the light field due to vibrations and potentially molecular rotations.

Classical Picture

In order to understand how molecular vibrations give rise to Raman scattering we now briefly review the basic idea behind the vibrational diatomic lattice model, as shown in figure 2.1. The diatomic model reduces a molecular vibration to the problem of two atoms connected by a spring and determines the modulation of the molecular polarisability due to the atoms' vibrations.

The electric field of the excitation light induces a dipole moment \mathbf{P} determined by the polarisability α . The relative motion of the atoms in the diatomic lattice causes an amplitude modulation of the polarisability at characteristic frequencies. Typically the modulation is small

compared to the inter-atomic distance, leading to a linear response in most cases.

In general the polarisability can be approximated by a power series expansion as follows

$$\alpha = \alpha_0 + \left. \frac{\partial \alpha}{\partial r_1} \right|_{r_1=0} r_1 + \left. \frac{\partial^2 \alpha}{\partial r_1 \partial r_2} \right|_{r_1, r_2=0} r_1 r_2 + \dots \quad (2.1)$$

Here $r_1 = r_0 \cos(2\pi\nu_1 t)$ and $r_2 = r_0 \cos(2\pi\nu_2 t)$ are two different vibrational modes with frequency ν_1 and ν_2 such that $\left. \frac{\partial \alpha}{\partial r_1} \right|_{r_1=0}$ and $\left. \frac{\partial^2 \alpha}{\partial r_1 \partial r_2} \right|_{r_1, r_2=0}$ are the first and second order Raman scattering contributions respectively [11]. This gives the first order dipole moment term to be,

$$\left. \frac{\partial \alpha}{\partial r_1} \right|_{r_1=0} \frac{r_0 E_0}{2} [\cos(2\pi(\nu_0 - \nu_1)t) + \cos(2\pi(\nu_0 + \nu_1)t)] \quad (2.2)$$

where the cosine term with frequency $\nu_0 - \nu_1$ is the Stokes and the $(\nu_0 + \nu_1)$ -term is the anti-Stokes line. Raman spectroscopy as a technique is based on the detection of stokes and anti-stokes signals. Under normal conditions the Stokes line is often the dominant signal hence in spectroscopy literature it is known as ‘the Raman line’. Equation 2.2 implies the selection condition $\left. \frac{\partial \alpha}{\partial r_1} \right|_{r_1=0} \neq 0$ necessary for the induced dipole moment and thus the vibrational mode to contribute to Raman scattering. This means vibrational modes must constitute a change in polarisability, with amplitude, to be ‘Raman active’.

Raman scattering not only occurs in molecules, but also in solids. There are no rotational Raman shifts only vibrational ones. In the solid state context vibrations are referred to as phonons. These phonons are quasiparticles that arise through quantisation of the classical vibrational modes of a solid. Like in the classical case, phonons can be ‘Raman active’ or ‘Raman inactive’.

The quantum description of the Raman scattering process can be separated into light-electron and electron-lattice interactions, and we can distinguish again between harmonic and anharmonic terms. Figure 2.2 represents a first-order (harmonic) Raman process. For describing temperature dependence of Raman line position and width anharmonic terms are important.

In the case of Stokes scattering, an excitation photon ω_E is absorbed into the material via electron excitation H_{RE} . This changes the electron potential between lattice atoms H_{RL} , inducing an optical phonon ω_P . The interaction with the phonon leads to a frequency shift of ω_P for the photon subsequently re-emitted by the solid, satisfying energy conservation.

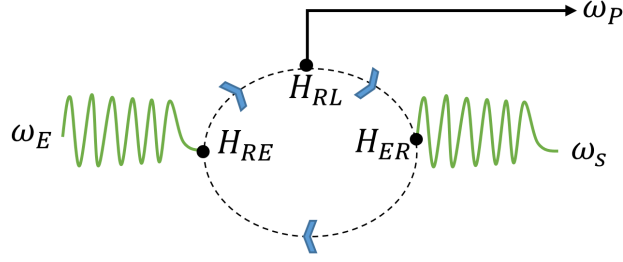


FIGURE 2.2: First order Raman scattering process. ω_E is incident excitation radiation, ω_P is the induced optical phonon, ω_S is the Stokes/Raman signal, H_{RE} is the radiation-electron interaction, H_{RL} is the radiation-lattice interaction and H_{ER} is the electron-radiation interaction [11].

Higher-order contributions to Raman scattering such as anharmonic interactions contribute significantly less to the scattering intensity, especially in a covalently bonded lattice (homopolar) such as diamond [12]. However, anharmonicities are important for investigating temperature-dependent Raman cross sections, as we will see later on.

Quantum mechanics introduces a time-energy uncertainty, and probabilistic interpretation of photon and phonon creation and annihilation events. Energy conservation remains satisfied, so the scattering process is the sum of all creation and annihilation event probabilities. The polarisability tensor is the central result of Raman scattering theory and directly reflects energy conservation through the resonant form, shown in equation 2.3.

$$\alpha_{nm} = \sum_E \left[\frac{\mathbf{P}_n^{E,L/R} \mathbf{P}_m^{R,E}}{H_{RE} - \hbar ck} + \frac{\mathbf{P}_m^{E,L/R} \mathbf{P}_n^{R,E}}{H_{RE} + \hbar ck'} \right] \quad (2.3)$$

This form of the equation is usually denoted Kramers, Heisenberg and Dirac (KHD) form [13]. Here, α_{nm} is the 3×3 polarisability tensor for the first order Raman scattering process. $\mathbf{P}^{E,L/R}, \mathbf{P}^{R,E}$ are the transition dipole moments from electron to lattice/Stokes-radiation interaction and radiation to electron interaction respectively. H_{RE} is the radiation to electron interaction energy as shown in figure 2.2. k, k' are the incident and radiated wave-vectors respectively. The polarisability tensor is summed over all electron interactions (E) possibilities consistent with energy conservation.

Following the description of Jayasooriya and Jenkins in Chapter 3 of ‘*An Introduction to Laser Spectroscopy*’ [14], we separate the molecular state into its vibrational and electronic components:

$$|M_n\rangle = |\psi_n\rangle |\phi_{n\nu}^x\rangle \quad (2.4)$$

M_n is the state of the n^{th} molecule with electronic and vibrational components ψ_n and $\phi_{n\nu}^x$ respectively, where ν is the vibrational frequency of the mode, x is the co-ordinate of vibration. Applying equation 2.4 to the polarisability tensor (equation 2.3) we get,

$$\alpha_{nm}^{\nu,\nu'} = \sum_E \left[\frac{\langle \phi_{0,\nu}^x | \mathbf{P}_n^{E,L/R} | \phi_E^x \rangle \langle \phi_E^x | \mathbf{P}_m^{R,E} | \phi_{0,\nu'}^x \rangle}{H_{RE} - \hbar ck} + \frac{\langle \phi_{0,\nu}^x | \mathbf{P}_m^{E,L/R} | \phi_E^x \rangle \langle \phi_E^x | \mathbf{P}_n^{R,E} | \phi_{0,\nu'}^x \rangle}{H_{RE} + \hbar ck'} \right] \quad (2.5)$$

$$\Rightarrow \alpha_{nm}^{\nu,\nu'} = \langle \phi_{0,\nu}^x | \sum_E \left[\frac{\mathbf{P}_n^{E,0}(Q_x) \mathbf{P}_m^{0,E}(Q_x)}{H_{RE} - \hbar ck} + \frac{\mathbf{P}_m^{E,0}(Q_x) \mathbf{P}_n^{0,E}(Q_x)}{H_{RE} + \hbar ck'} \right] | \phi_{0,\nu'}^x \rangle \quad (2.6)$$

$$= \langle \phi_{0,\nu'}^x | \alpha_{nm}^{[0,0]}(Q_x) | \phi_{0,\nu}^x \rangle \quad (2.7)$$

In equation 2.6 we assume Raman scattering only from the vibrational and electronic ground state $|0,0\rangle$ [14, 15].

As in the classical picture, vibrational modes cause only small changes in the translational dipole moment. We again employ the small amplitude approximation taking the series expansion about Q_0 the vibrational equilibrium co-ordinate.

$$\alpha_{nm}^{\nu,\nu'}(Q_x) = \alpha_{nm}(Q_x) \delta_{\nu,\nu'} + \left. \frac{\partial \alpha_{nm}}{\partial Q_x} \right|_{Q_0} \langle \phi_{0,\nu}^x | (Q_x - Q_0) | \phi_{0,\nu'}^x \rangle + \dots \quad (2.8)$$

The Dirac brackets imply a symmetry selection rule, with only transitions satisfying $\nu = \nu' \pm 1$ (involving one quantum of energy) contributing to Raman scattering. As before the derivative of the polarisability with respect to the vibrational co-ordinate must not vanish around its equilibrium position (when $Q_x = Q_0$).

2.1.2 Raman Scattering Properties

Equipped with the main results of Raman scattering theory we now move to investigate fundamental properties of Raman scattering.

Wavelength Dependence

The intensity I of the Raman scattered photons, as with Rayleigh scattering, scales as $I \propto \frac{1}{\lambda^4}$. Excitation with short-wavelength or high-energy light improves the signal to noise-ratio, with equations 2.3, 2.10 and 2.12 following the $\propto \frac{1}{\lambda^4}$ wavelength dependence.

Investigations have looked into wavelength dependence of the Raman scattering cross-section using different gas species. Employing wavelength sources in the range 200-600nm the wavelength and scattering cross-sections were characterised and compared with theory, showing agreement within 10% [16].

Polarisation Dependence

Considering equation 2.3 which relates the components of the incident electric field to induced polarisation components. We separate α_{nm} into a sum of its Raman polarisability tensors [17],

$$|\alpha_{nm}|^2 = \sum_k |\mathbf{e}_i R_{ij}^k \mathbf{e}_j|^2 \quad (2.9)$$

for $\mathbf{e}_{i,j}$ polarisation vectors and R_{ij}^k the k^{th} polarisability tensor. Each α_{ij} element of R_{ij}^k , an electric field in the j^{th} direction will polarise in the i^{th} direction. Diagonal elements represent the Raman scattering in the direction of the applied electric field and R_{ij}^k can be separated into Raman tensors over species-specific lattice orientations. For example, diamond has nine characteristic polarisability tensors R_{ij}^k over its cubic lattice orientations, which is discussed in more detail in the following section.

Scattering Cross-Section

Scattering cross-section is the probability that an incident photon is scattered into a unit solid angle, otherwise described as photon flux or scattering rate over a solid angle. For Raman scattering, this is represented by the Kramer-Heisenberg dispersion equation [14, 18].

$$\frac{d\sigma}{d\Omega} = \frac{kk'}{16\pi^2\epsilon_0^2} |\alpha_{nm}|^2 \quad (2.10)$$

where k and k' are incident and scattered wavenumbers respectively, ϵ_0 is the permeability of free space and α_{nm} is the polarisability tensor (equation 2.3). Integrating over all space gives the total scattering cross-section.

The scattering cross-section is proportional to photon flux and thus laser field and scattered Raman intensity (or power). We can therefore write the differential cross-section in the more applicable form [18]

$$d\sigma = \frac{P_R}{P_L} N l \Omega = \frac{I_R \lambda_L}{I_L \lambda_R} N l \Omega \quad (2.11)$$

where P_R and P_L are the Raman and laser powers, while I_R , I_L and λ_L , λ_R are the Raman and laser intensities and wavelengths respectively. N is the number of molecules intercepted, l is the detected beam width and Ω is the scattering solid angle.

The scattered Raman power P_R parameters include polar and azimuthal angle co-ordinates (θ, ϕ) , scattering solid angle Ω and wavelength. P_R is proportional to laser power, unit cross section, number of intercepted molecules, detected beam width and solid angle.

Scattering Efficiency

Normalisation of the Raman scattering cross-section by cross sectional area, yields the dimensionless scattering efficiency coefficient S (usually also denoted as scattering matrix). Scattering efficiency is the ratio of scattered power to incident power intercepted by the cross-section area. It is polarisation, frequency, species, beam width, spot size and power dependent and is given by [11]

$$S = \frac{2\hbar w_s^4 N^2}{\rho c^4 \Omega} (\tilde{n}(\nu_0, T) + 1) |\alpha_{nm}|^2 \quad (2.12)$$

w_s is the scattering frequency, N is the number of molecules per unit volume intercepted by the laser beam, ρ is the species density, Ω is the solid angle, $\tilde{n}(\nu_0, T)$ is the Bose-Einstein distribution function and α_{nm} the Raman polarisation tensor (as in equation 2.3) [19]. S is a dimensionless quantity with higher values implying improved scattered to incident photon flux ratio through Ω .

2.2 Diamond

Unique in many ways and with outstanding material properties, diamond provides a versatile platform for implementing novel optical, electronic and quantum technologies. The diamond field has seen a tremendous boom of applications over the past decade.

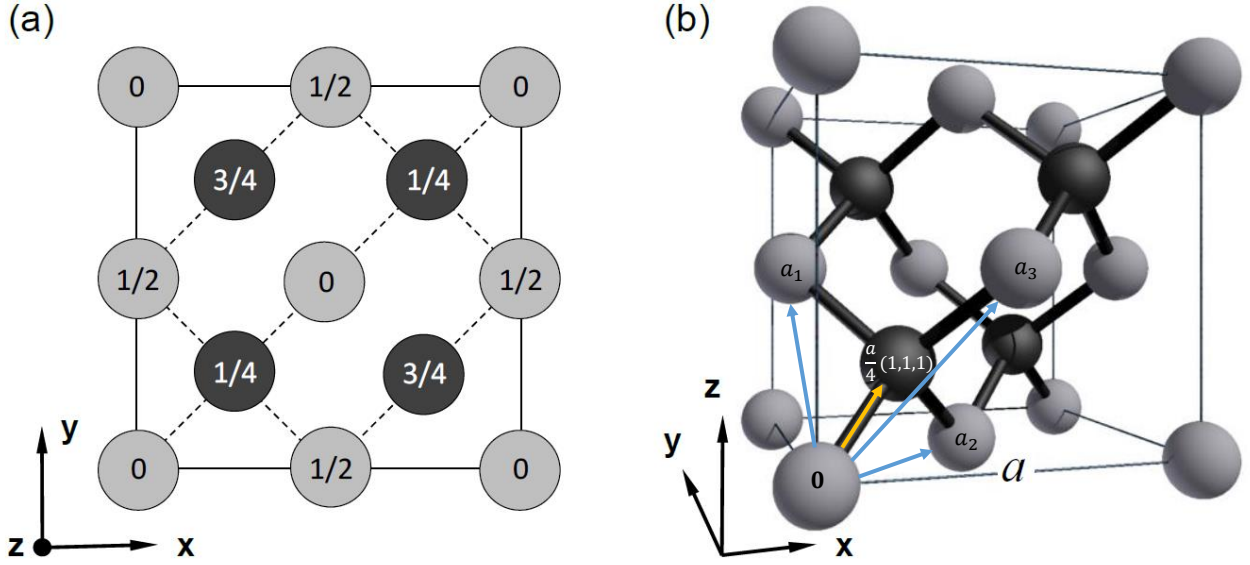


FIGURE 2.3: Cubic unit cell of a diamond lattice, adapted from [22]. (a) 2-dimensional cross-section, each number represents the carbon atoms position scaling in the unit cell. (b) 3-dimensional representation, $\mathbf{0}$ and $\frac{a}{4}(1,1,1)$ are the basis points, a_1 , a_2 and a_3 are the Bravais lattice vectors for which translations remain invariant. $a = 0.356$ nm while nearest neighbours are 0.154 nm apart at ambient temperature [22].

2.2.1 Properties of Diamond

Crystallographic Properties

The carbon atoms in the diamond lattice have sp^3 -hybridisation and therefore form strong covalent bonds in a tetrahedral structure [20]. The lattice structure of diamond can be thought of as a face-centered cubic ‘*fcc*’ lattice with a two-atom basis. Each carbon atom has four neighbouring carbon atoms. Hence the diamond lattice consists of two *fcc* displaced along the diagonal (yellow arrow in figure 2.3). Note that the tetragonal diamond lattice structure itself is not a Bravais lattice but can be reduced to two interpenetrating ‘*fcc*’ Bravais lattices [21].

Electronic Band Gap Properties

Diamond is one of the best insulators available with an indirect electronic band gap of 5.4 eV and 7.5 eV direct band gap [23, 24]. Comparing to technologically relevant semiconductor material

such as GaN which has a direct band gap of 3.4 eV and excitation wavelength at approximately 365 nm (near UV). The excitation wavelength for diamond is in the deep UV, namely 165 nm [25], making diamond an ideal material for high power semiconductor applications.

Thermal Properties

Pure crystalline diamond can reach a thermal conductivity of $22 \text{ Wcm}^{-1}\text{K}^{-1}$ due to the nature of valence electron sharing in a covalently bonded lattice [26, 27]. In comparison, Copper and GaN thermal conductivities are $4 \text{ Wcm}^{-1}\text{K}^{-1}$ and $1.3 \text{ Wcm}^{-1}\text{K}^{-1}$ or 5 and 17 times smaller than diamond, respectively [28]. Diamond has a specific heat capacity of $6.195 \text{ J/mol}\cdot\text{K}$ at 300 K [29]. This is low compared to the specific heat capacity of GaN of $35.5 \text{ J/mol}\cdot\text{K}$ at 300 K, meaning GaN is a better thermal insulator compared to diamond which requires 6 times less energy to increase in temperature by one degree.

The thermal expansion constant in diamond ranges from $0 - 3 \times 10^{-6} \text{ K}^{-1}$ over the range 0-500 K and at room temperature is approximately $1 \times 10^{-6} \text{ K}^{-1}$ [30, 31]. This is 2.5 and 3 times smaller than crystalline Silicon and GaN which have expansion coefficients $2.6 \times 10^{-6} \text{ K}^{-1}$ and $3.1 \times 10^{-6} \text{ K}^{-1}$ respectively [32, 33]. This implies that the diamond lattice is tightly bound and able to maintain a solid phase at high temperatures, consistent with its high melting point at 4500 K [34].

Diamond has a high Debye temperature of 1960 K (almost half its melting point temperature), the temperature required to excite all phonon modes [35]. For comparison, Copper and GaN have Debye temperatures of 310 K and 1000 K respectively [36, 37]. Higher Debye temperatures imply higher density of states at higher phonon frequencies, and thus generally a 'stiffer' material, which is the case for diamond.

Optical Properties

Pure diamond is considered to be optically transparent, with a 70% transmission in the wavelength range from 225-2000 nm and for wavelengths greater than 6000 nm. In the IR range 2000nm-6000nm, carbon-carbon absorption causes transmission to drop to 50% [38]. Diamond has a relatively high dispersion coefficient of $dn/d\lambda = 0.044 \text{ 1/nm}$, approximately double that

TABLE 2.1: The thermal properties of diamond as experimentally measured at ambient temperature unless otherwise specified.

Properties	Values	References
Band Gap (Indirect, Direct)	5.4 eV, 7.5 eV	[23, 24]
Thermal Conductivity	22 Wcm ⁻¹ K ⁻¹	[26]
Specific Heat Capacity	6.195 J/mol ·K	[29]
Thermal Expansion	From 0-500 K: $0 - 3 \times 10^{-6}$ K ⁻¹	[30]
Debye Temperature	1960 K	[35]
Melting Point	≈ 4500 K	[34]

of glass given a refractive index change of 2.42-2.46 over 390-750nm wavelength range [39, 40]. This gives diamond its characteristic sparkle as multi-wavelength or continuous light is dispersed into its monochromatic components.

The NV Defect in Diamond

Not all diamond species appear clear and transparent, with possible colours over almost the entire visible spectrum such as pink, brown, orange or blue [41]. The characteristic diamond colour is caused by impurities and/or defects (more commonly called colour centers) where an atom of the carbon lattice is replaced with a different atom and/or a vacancy [39]. The most common and best-understood colour centre in diamond is the Nitrogen-vacancy (NV) defect. It consists of a molecular complex, which is formed when one carbon atom is replaced by a nitrogen atom with an adjacent vacancy site, illustrated in figure 2.4.

The NV defect in a diamond lattice unit cell has threefold rotational symmetry around the [111] axis, as described by the C_{3v} cyclic group of three elements [22]. The NV center is interpreted to act as an artificial atom with an atom-like level structure which allows for optical addressing and readout. The NV center has two possible charge configurations: neutral and negative, NV^0 and NV^- , having different zero phonon lines (ZPL) at 575nm and 637nm wavelengths respectively [42]. The NV^- is the most common charge state (six electrons) of an NV center as NV^0 require local environment conditions allowing the donation of an electron from NV^- to another location, producing NV^0 with only five electrons. Its basic energy level

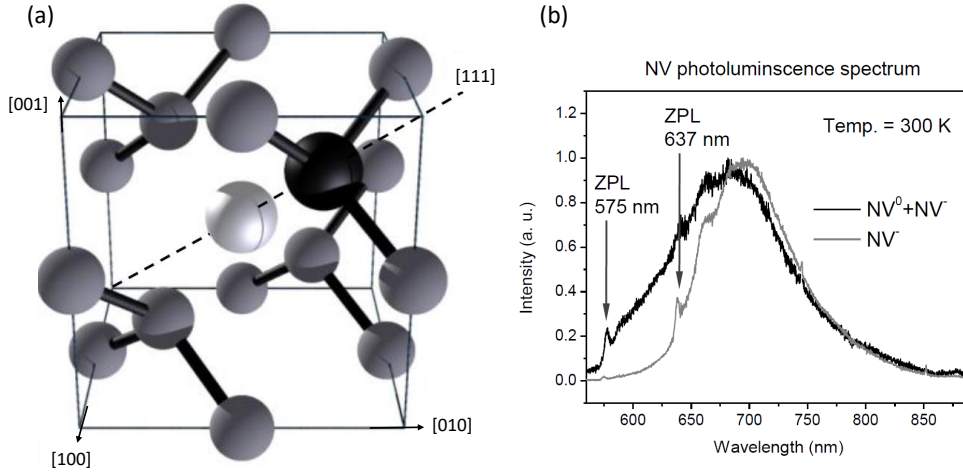


FIGURE 2.4: Representation of the (a) NV center in a diamond lattice unit cell and (b) the NV^- and NV^0 photoluminescence spectra. The dark and light points representing the nitrogen and vacancy center respectively. Here [100], [010] and [001] are the usual x,y,z lattice vectors. This figure is adapted from [22].

structure is displayed in figure 2.5.

In figure 2.5 $D = 2.88$ GHz is the energy difference between the $m_s = 0$ and $m_s = \pm 1$ (doubly degenerate state, assuming no external magnetic field) spin ground states at room temperature. As we will discuss later $D = D(T)$ is temperature dependent and can be readout using optically detected magnetic resonance (ODMR).

2.2.2 Raman Scattering from Diamond

The Raman spectrum of diamond was first measured in 1930 using early IR spectroscopy techniques [43]. In fact, diamond was one of the first materials to have its Raman spectrum measured, likely motivated by diamond having a high Raman scattering efficiency able to be detected/imaged by early spectrograph equipment.

The Raman peak position was first measured to be at 1332 cm^{-1} by Ramaswamy in 1930 and further investigation of various diamond species done by Bhagavantam [44, 45]. Robertson and Fox in 1934 measured the Raman spectrum with two different types of uncategorised but visually distinguishable diamond samples. They found the Raman peak deviated slightly from

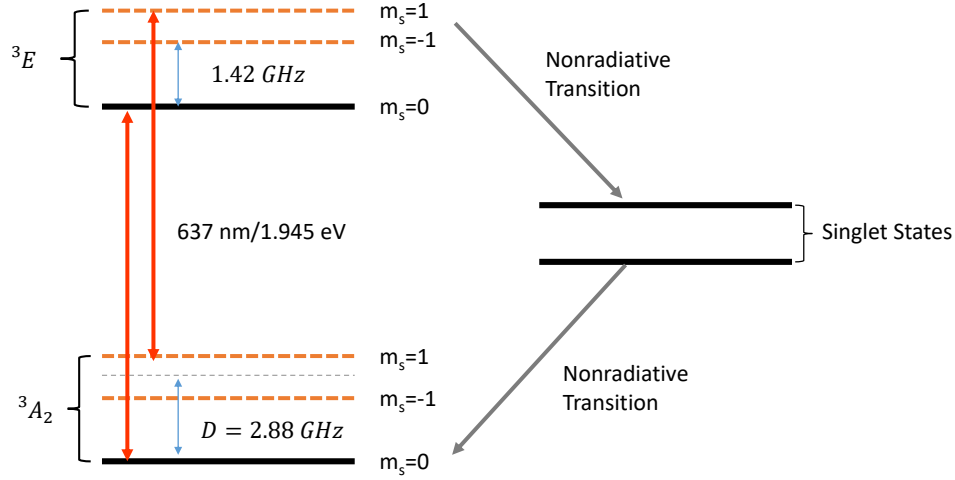


FIGURE 2.5: NV⁻ energy level configuration in diamond. The red lines are spin conserving 637 nm dipole transitions. The orange energy levels represent the ground (3A_2) and excited (3E) spin states with D being the frequency splitting ($m_s = \pm 1$) at room temperature. The $m_s = \pm 1$ states are degenerate with no external magnetic field. Inter-system crossing to the singlet levels provides a non-radiative decay path that initialises the spin into the $m_s = 0$ state.

the expected 1333.2 cm^{-1} position for pure diamond [46].

Based on these early experiments, the theory was developed to a point where measured and predicted Raman spectra could be compared. In 1934, using classical crystal dynamics, Nath was able to derive a frequency expression for the triply degenerate Raman frequency mode with a theory value of 1346 cm^{-1} for the Raman shift, while describing its cause through ‘*The origin of the principal Raman frequency is due to the vibration of the two lattices relative to one another, each being considered as rigid*’ [47]. In other words, the Raman frequency originates from the vibration between the two interpenetrating ‘fcc’ rigid sub-lattices of diamond in 3 possible directions. Theory and experimental investigations into the Raman spectra of diamond continued, developed by Krishnan, Raman, Nayar and others [48–51].

The 1950’s and 1960’s saw the development of higher order anharmonic Raman scattering theories, with emphasis based around diamond/cubic structured materials. Klemens investigated anharmonic lattice interaction theory by considering local lattice vibrations caused by

lattice defects. The anharmonic interaction is assumed to originate from a 3 phonon interaction with the local (presumably optical) phonon decaying into two acoustical phonons. Starting from a perturbation Hamiltonian and second order perturbation theory, Klemens found an expression for the inverse phonon relaxation time with a temperature dependence factor $N'' + N' + 1$ [52]. N'' and N' are Bose-Einstein factors which represent the equilibrium occupation numbers of the modes \mathbf{k}'' and \mathbf{k}' which interact with the optical mode. Further developments by Klemens introduced the overtone approximation $w'' = w' = w/2$ where w is the original optical phonon frequency. Then the temperature dependence factor is $2N + 1$, forming the basis of the Klemens model for thermal Raman dependence [53]. With increasing temperature the thermal occupation factor increases along with the inverse relaxation time, causing shorter phonon decay times.

However, Klemens overtone approximation does not account for non-overtone decay branches. A review study by Menendez shows that almost half of the phonon decay paths in diamond are overtone processes. However, for silicon and germanium the number of overtone decay paths is an order of magnitude smaller than non-overtone decay paths so the Klemens approximation would not sufficiently describe the Raman thermal dependence of these materials [54].

Alternatively, Cowley developed a theory to explain Raman scattering from diamond like crystals, employing the use of the Shell Model for harmonic frequency calculations and anharmonics for nearest neighbours. Based on one and two phonon interactions and starting from the Raman polarisability dependence, Cowley is able to determine the Raman polarisability matrix elements. This leads to temperature dependent expression for one and two phonon interactions and simulated calculations of the peak shift and inverse phonon decay time (linewidth) at different temperatures of Germanium [55].

It should be noted that Klemens anharmonic decay model and Cowleys harmonic shell description with anharmonic nearest neighbour coupling were motivated by the work of Loudon. He did extensive investigations into the polarisation dependence of Raman scattering efficiency with various structured elements including diamond [11].

Anharmonicities describe the temperature dependent processes that cause the Raman linewidth dispersion and peak position shift to higher frequency, as described in the next section.

2.3 Raman Thermal Characteristics

2.3.1 Line Shift Temperature Dependence

The Raman scattering cross-section for longitudinal optical (LO) phonons has a resonant frequency term with a temperature dependent frequency shift constant [56]. The frequency shift is proportional to a principle factor containing the temperature dependence in a sum of Bose-Einstein factors, the size of which is dependent on the number of phonons assumed in the process [54, 56]. The 3-phonon process (one optical phonon decaying into two acoustical/thermal phonons in the LO mode) is given by

$$\Omega(T) = \Omega(0) \left(1 + \frac{2}{e^{\hbar w/2k_B T} - 1} \right) \quad (2.13)$$

where $\Omega(0)$ is the the peak shift at 0 K, w is the Raman active optical phonon frequency and \hbar, k_B are the usual constants.

The form of equation 2.13 has been extended include 4-phonon processes, the decay of an optical phonon into 3 acoustical/thermal phonons giving

$$\Omega(T) = \Omega(0) + A \left(1 + \frac{2}{e^{\hbar w/2k_B T} - 1} \right) + B \left(1 + \frac{3}{e^{(\hbar w/3k_B T)^2} - 1} + \frac{3}{e^{(\hbar w/3k_B T)} - 1} \right) \quad (2.14)$$

A and B are fitting parameters [56].

The three and four phonon decay models (equations 2.13 and 2.14) are able describe low temperature changes in the Raman line. However, at high temperatures the 3-phonon decay model does not account for additional contributions from 4-phonon decay effects. Experimentally we are limited to ~ 500 K so higher order phonon decay effects are insignificant [56] over this temperature range.

2.3.2 Linewidth Temperature Dependence

Similarly, the peak width is governed by the decay time of the LO phonon into longitudinal acoustical (LA) phonons. Klemens regarded the two LA (w_1, w_2) phonons to sweep the frequencies between $0 - \Omega(0)$ and $\Omega(0) - w_1$. This accounts for the Raman line width, while a temperature increase causes the contributing frequency range to increase.

For the three and four phonon processes we have [56]

$$\Gamma(T) = \Gamma(0) \left(1 + \frac{2}{e^{\hbar\omega/2k_B T}} \right) \quad (2.15)$$

$$\Gamma(T) = \Gamma(0) + A \left(1 + \frac{2}{e^{B\hbar\omega/2k_B T} - 1} \right) + B \left(1 + \frac{3}{e^{(\hbar\omega/3k_B T)^2} - 1} + \frac{3}{e^{(\hbar\omega/3k_B T)} - 1} \right) \quad (2.16)$$

The thermal dependence is identical to that of peak position since it comes about from a proportionality dependence of the Raman scattering cross section [54, 56].

2.3.3 Fluorescence Temperature Dependence

Besides Raman peak shifts and linewidths, the intensity ratio of Stokes versus Anti-Stokes line can be used to extract the temperature of the sample. The ratio is exponentially dependent on temperature and is given by

$$\frac{I_{AS}}{I_S} = \left(\frac{w_i + w_p}{w_i - w_p} \right)^4 \gamma e^{\frac{\hbar w_p}{k_B T}} \quad (2.17)$$

where I_{AS} and I_S are the Anti-Stokes and Stokes intensities, w_i, w_p are the incident photon and phonon frequencies, respectively. The first term accounts for the scattering cross section frequency dependence. γ is the correction factor for the detection efficiency and usually taken as a constant [57].

Measuring this ratio tends to provide more consistent results compared to just the intensity change of the Stokes line with temperature, which requires very good baseline fluorescence stability. The Stokes anti-Stokes intensity ratio for diamond was first measured by Krishnan where he achieved good agreement between theory and experimental values [58]. However, later experimental studies demonstrated a systematic deviation of the experiment from the theoretical expectation even when correcting for absorption [56, 59]. It was shown that for temperatures above 750 K, the systematic error of the Stokes/Anti-Stokes ratio becomes significant. The cause has been attributed to thermal dependences of the instrumentation and the diamond sample itself.

TABLE 2.2: List of all the significant Raman thermometry characterisation studies with diamond. N/S implies the information was not specified and S-AS is the Stokes Anti-Stokes ratio.

Author-Date	Diamond Species	Thermal Measurements	Temperature Range	Excitation Source-Power	Resolution	References
Krishnan-1946	Bulk-Type: N/S	Peak frequency shift, FWHM	358-1249 K	253.7 nm- Power: N/S	N/S	[60]
Borer-1971	Bulk-Type I, II and Synthetic	Peak frequency shift, Half Width	25-1000 K	488 nm- Power: N/S	N/S	[61]
Anastassakia-1971	Bulk-Type IIa	Peak frequency shift, FWHM, S-AS	10-1000 K	633 nm-Power: 25mW	Spectral resolution: 1 cm^{-1}	[62]
Zouboulis-1991	Bulk-Type: N/S	Peak frequency shift, FWHM	300-1900 K	406.7 nm- Power: N/S	Thermal resolution: $\sim 10 \text{ K}$	[63]
Herchen-1991	Bulk-Type IIa	Peak frequency shift, FWHM, S-AS	293-1850 K	458 nm-Power: N/S	Spectral resolution: 0.1 nm	[59]
Cui-1998	Bulk-Type IIb, CVD	Peak frequency shift, S-AS	300-2000 K	488 nm-Power: N/S	Thermal resolution: $\sim 10 \text{ K}$ Spectral Resolution: 2 cm^{-1}	[57]
Liu-2000	Bulk-Type IIa	Peak frequency shift, FWHM	77-873 K	514.5 nm-Power: N/S	Thermal resolution: 5 K Spectral resolution: 0.2 cm^{-1}	[64]

2.4 Raman Thermometry with Diamond

2.4.1 Bulk Diamond Thermometry

Raman thermometry with bulk diamond species have been experimentally studied for the past 60-70 years. Krishnan gave the first thermometry results for diamond where he observed the Raman peak shift of 15 cm^{-1} between 85°C and 976°C degrees [60]. There was little motivation to reproduce this experiment until the advent of the laser in the 1960's, as exposure times as long as 2 hours were required to observe the Raman signal. The Raman peak position and width temperature dependence was remeasured in 1970 using early argon ($\lambda = 488\text{nm}$) and He-Ne ($\lambda = 638\text{nm}$) lasers, over the 10—1000 K temperature range [61, 62]. During the early to late 1990's Raman thermometry studies of diamond were conducted with temperature ranges up to 2000 K, close to the Debye temperature [63]. Cui in 1998 was the first to measure the Raman temperature dependence of chemical vapor deposition (CVD) diamond [57]. While Liu in 2000 performed micro-Raman thermometry of diamond with an effective scattering region of $2.5 \text{ }\mu\text{m}$ by $5 \text{ }\mu\text{m}$, from 77-873 K [64].

2.4.2 Nano-Scale Diamond Thermometry

There has been little motivation to seriously characterise the Raman thermal dependence of nanodiamond (ND). Nanocrystalline diamond can be effectively treated as bulk material for sizes above 20—50nm [65, 66]. This is described as the Gaussian Confinement Effect which predicts an uncertainty in the optical phonon wave vector of $\Delta q \sim \pi/d$ for a material grain of

size d [67]. For ND sizes below 20 nm the relative Raman peak position and broadening effects due to phonon confinement are difficult to account for, especially if the grain boundaries need to be quantified. However, we do not use NDs below 100nm in this investigation, making a detailed description of the phonon confinement effect unnecessary.

2.5 Alternate Thermometry Methods in Diamond

Nanoscale thermometry from diamond is not limited to interpretations of the Raman effect. Colour centers such as, the NV^- and Silicon vacancy (SiV^-) centers in diamond provide optical transitions that can yield temperature information.

2.5.1 NV-Spin Temperature Sensing

Temperature sensing with the NV center makes use of the ground state spin, which has a zero-field splitting of D between the $m_s = 0$ and $m_s = \pm 1$ projections, as shown in figure 2.6. The temperature dependence of $D(T)$ is due to localised thermal lattice expansion around the NV^- centres, thus $D(T)$ is expected to change linearly with temperature [68, 69]. The application of microwaves resonant to D causes transfer between the spin states, which is visible as a contrast in the photoluminescence (PL) intensity. Sweeping the microwave frequency and monitoring the PL intensity produces an ODMR spectrum, from which the D resonance can be readout.

The width of the ODMR resonance may be limited by the spin coherence time of the NV center, and so extending this can improve the temperature resolution. This can be achieved by applying the microwaves in controlled pulses to dynamically manipulate the spin. Coherence times represent the Rabi oscillation duration (state evolution time), and increase the sensitivity of the temperature measurement, resulting from better signal to noise ratio [71]. Microwave pulse sequences employed to increase coherence time include:

- Hahn Echo pulse sequence: Initialises from $m_s = 0$ to $m_s = 1$ spin state by a π pulse, and the evolution time τ back to the $m_s = 0$ is readout.
- Thermal Echo pulse sequence similar to the Hahn Echo manipulates the spin from $m_s = 0$ to $m_s = -1$ and $m_s = 0$ to $m_s = 1$, assuming a static external field. This is achieved by

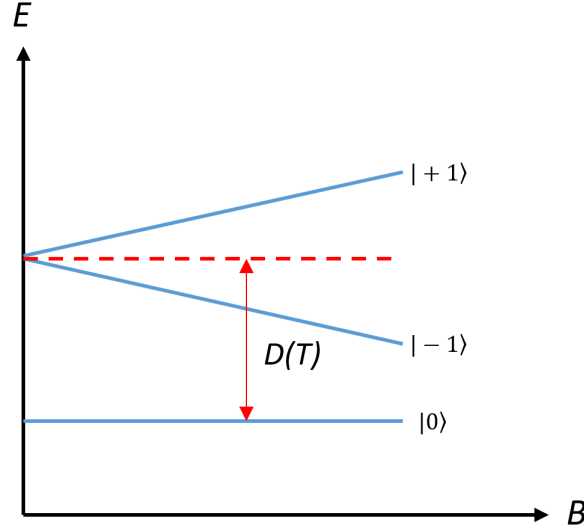


FIGURE 2.6: Zeeman diagram of the triplet NV^- ground state. With $|\pm 1\rangle$ the zero-field doubly degenerate state. Red dashed line is the zero field line and its frequency $D(T)$ from $|0\rangle$ is temperature dependent [70].

two sequences of triple π pulses.

- TCPMG-N (Thermal Carr-Purcell-Meiboom-Gill) pulse sequences which are similar to TE pulse sequences except they flip the spin $2N$ more times increasing the coherence time.
- CPMG-N is a subsequence of the TCPMG-N sequence which only performs N spin flips, having short coherence times compared to TCPMG-N.

The sensitivity achieved by NV^- thermometry is very high, examples include $130 \frac{\text{mK}}{\sqrt{\text{Hz}}}$ or ~ 1 K for high purity nanodiamond and using a TCPMG-8 pulse sequence thermal sensitivities of $10.1 \frac{\text{mK}}{\sqrt{\text{Hz}}}$ or ~ 2 mK have been achieved [70, 72]. These are significant improvements compared to resolutions achieved by Raman thermometry methods, as can be seen by comparison with table 2.2. This method requires system sensitivity, calibration and setup processes that are significantly more difficult, requiring high fluoresce detection efficiency and the isolation and addressing of single NV^- in diamond. For industrial applications where cost and complexity are more severe penalties than reduced thermal resolution, Raman thermometry with nanodiamond remains an attractive option for nano-scale temperature sensing.

2.5.2 SiV Temperature Sensing

The Silicon vacancy center in diamond has gained significant attention as an alternative to the NV center in recent years, especially on the basis of its superb optical photoluminescence properties [73, 74]. SiV^- is a spin half system with the spin remaining degenerate in the absence of a magnetic field, and therefore does not provide ODMR spin temperature sensing. However, the ground and excited states of SiV^- both have two-fold orbital degeneracy, which is lifted by spin-orbit interaction to produce quite large splittings [75]. At low temperature ranges (below about 100 K) when the fine-structure of the ZPL can be resolved, the intensity of PL transitions provide information about the thermal Boltzmann population distribution in the excited state. This can be used for thermometry, although the exact orbital splitting depends on transverse strain and so individual calibration would be required for each SiV^- center. This technique is not available at ambient conditions, since the ZPL transitions are thermally broadened and the fine structure cannot be resolved.

There is a thermal shift in the optical frequency of the ZPL that could in principle be used for thermometry [2, 76–78]. However this shift is also sensitive to strain along the SiV^- symmetry axis and so the calibration problem remains. It has also been reported that the excited state lifetime changes with temperature, and this could be used as a temperature readout alternative [79]. Application of the SiV centre in practical temperature sensing is yet to be established.

Thermometry techniques that build on the optical transitions of specific colour centers in diamond have one other key disadvantage for general applications. The optical wavelengths of interest are fixed by the colour center, and may fall into awkward absorption/ionisation bands of the device to be studied. The Raman line has a position shifted relatively from the excitation laser, and so the wavelengths of interest can be freely selected by choosing appropriate illuminations sources.

2.6 Applications to Electronic Devices

Conventional micro Raman thermometry has been utilised as an optical alternative to standard resistance temperature measurements. It enables Raman temperature readout of regions

inaccessible by resistance thermometry. An example relevant to this thesis is Raman thermometry on GaN and Aluminium Gallium Nitride (AlGaN) High Electron Mobility Transistors (HEMTs). They employed a modulated a 532 nm frequency doubled diode laser (pulsed) which was pulse synchronised optically (10-15 ns) and electrically (200 ns at 3.5-6 W), the GaN, AlGaN, SiC and Sapphire Raman signals were measured over 300-350 ns. The heating regime caused by the electrical pulse and cooling regime after the pulse was measured producing a peak temperature representative of the local maximum temperature in the measurement region [80].

A similar investigation comparing Raman and IR thermometry and thermal mapping has been conducted. It demonstrated the order of magnitude increase in spacial resolution of Raman thermometry compared to IR, based on the diffraction limits of the 488 nm laser and 2-5 μm IR sources. IR showed to have better depth of field (DoF) by an order of magnitude, due to IR being less absorbent. The IR temperature resolution represented better sensitivity, but IR temperature measurements are spatially averaged over larger regions, compared to Raman temperatures [81].

Micro-scale thermometry with diamond on GaN and AlGaN HEMT gates has been demonstrated. A micron sized diamond was placed on a T-gate and T-gate field plate acting as a micro scale Raman thermometer. Temporal resolutions of 10 μs were demonstrated, any shorter and the micro-diamond might not have been in thermal equilibrium. The T-gate electrical pulse power was 6 W/mm and 7 W/mm for the field plate T-gate for 10 μs pulses. For the T-gate the diamond came within 10° of the simulated peak gate temperature a 30° improvement on conventional Raman thermometry coming only within 50° of the peak temperature. The field plate gate limited the heat transfer to the diamond, causing a peak Raman temperature within 30° of the simulated peak temperature, while the conventional Raman thermometry of the GaN remained relatively the same as the T-gate measurement [1].

This thesis takes the concept of micro-Raman thermometry into the nano-scale regime, making use of the high-quality nanodiamond size sorting and processing at Macquarie University.

3

Methodology

This chapter describes the experimental process and solutions employed to address the challenge of locating and addressing single 250 nm nanodiamonds. The general concept of confocal microscopy is introduced along with a detailed description of our lab-built confocal microscope.

3.1 Confocal Microscopy

‘Confocal’ means ‘together-focus’, and for a microscopy application, the illumination and detected fluorescence are both focused by the same optical components. The idea is to detect fluorescence from the same sample region that is illuminated. Confocal microscopy as described by ray optics is a single point detection of a sample, although in actuality there is a detection volume. This volume is parameterised by the Abbe diffraction limit in the lateral

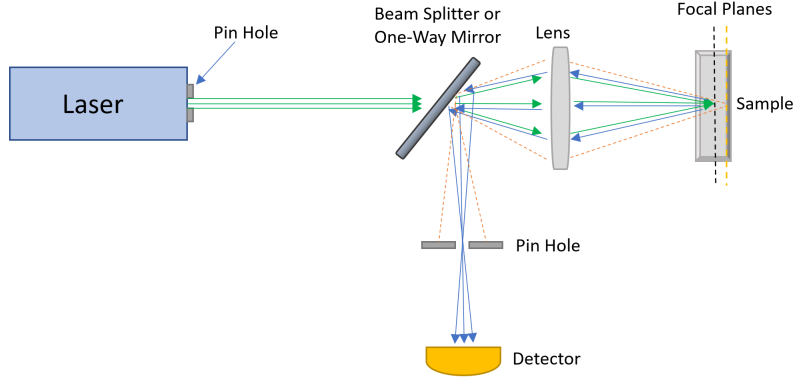


FIGURE 3.1: Conceptual ray optics diagram of a confocal microscope. Light that is not in the focal plane of interest (orange dashed lines) is not detected. The reflected light (blue arrows) is reflected from a point of interest on the sample, focused through a pin hole and detected.

directions by,

$$D_{lat} = \frac{0.44\lambda}{NA} \quad (3.1)$$

and in the axial direction by,

$$D_{axial} = \frac{1.5n\lambda}{NA^2} \quad (3.2)$$

generating a focal slice or 2-dimensional plane in ray optics [82]. Confocal microscopy can be described by the concept of a point spread function (PSF) which is the detected signal of a point like object. Each point object creates its own intensity PSF. The overall PSF (and intensity) of the illumination volume, is the product of point object PSFs, with the pin hole aperture size accounted for. Confocal microscopy has the advantage of lower background noise and higher special resolution, particularly in the axial direction, compared to wide field microscopy.

A confocal microscope requires a raster or other form of scan to generate a wider field of view image [82]. The image is generated pixel by pixel which can be a lengthy process at low photon counts. This can be improved with the use of intense light sources such as lasers.

Confocal microscopes are quite modular and can be adapted to particular experiments but the general concept remains the same. An example includes the reflection design used by Minsky [83] which places a mirror behind the sample or a transmission setup which detects light from the opposite (relative to excitation direction) side of the sample. However, the configuration used for this thesis is a reflection (without the mirror) confocal microscope, which collects only

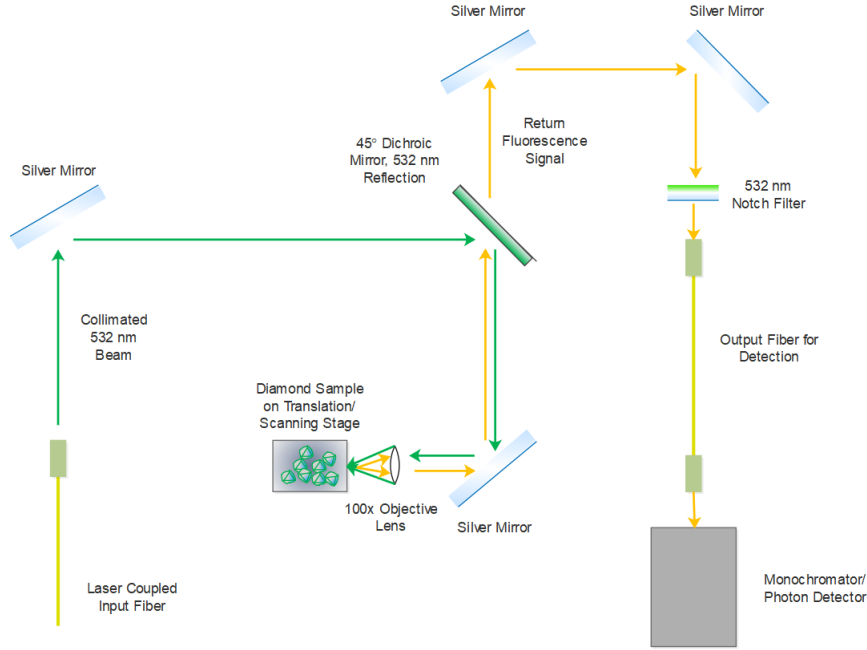


FIGURE 3.2: Generalised diagram of our lab built confocal system optimised for 532 nm excitation. The green arrows represent the 532 nm excitation beam, and the yellow/orange arrows represent the return fluorescence signal. The output fiber is manually swapped between the avalanche photo-detectors and the monochromator. The objective lens was mounted in a periscope configuration.

scattered light in the beam path direction.

3.2 Lab Built Confocal Microscope

A compact confocal imaging system mounted on a bread board was built with the intended capability of single nano-diamond and NV^- centre addressing. The system is designed to detect the bright NV^- fluorescence and diamond Raman signal at 572 nm from 532 nm excitation.

The beam path is controlled by wavelength appropriate single mode fibers (Thorlabs, P3-460B-FC), silver protected mirrors (Thorlabs, PF10-03-P01), Olympus $100\times$ inf/0/FN26.5 objective lens with numerical aperture (NA) 0.9 and a 45° 550nm cutoff dichroic mirror (Thorlabs, DMLP550). This reflects the 532nm beam for sample illumination and transmits the 572nm Raman and broad range 570-800 nm NV fluorescence signal. The 532 nm notch filter (Semrock NF01-532U-25) reduces the detected 1-2% laser scatter leakage from the dichroic. This means reduced laser scatter counts detected by the Avalanche Photo Diode (APD) photon detectors,

making Raman and fluorescence the dominant count source. The confocal microscope was operated using the Qudi software suite [84]

3.2.1 Resolution and Efficiency of Confocal System

The collection efficiency of the system is found by taking the sum of collection efficiencies for each component along the detection path, and is $\eta \sim 4\%$. The objective lens has a collection efficiency of $\eta_{obj} = 38\%$. While the remainder of losses came from the dichroic mirror ($\leq 1\%$ loss), silver mirrors ($\leq 2.5\%$ loss), single mode fiber (70 % coupling loss, 6% attenuation loss), 1200 g/mm grating (50% loss), CCD camera (10 % loss).

The spacial resolution of the system for 532 nm source is laterally, ~ 260 nm from equation 3.1 and axially $\sim 1 \mu\text{m}$, determined by the diffraction limits. Both the Raman signal and NV fluorescence is emitted isotropically (equally in all directions), so relative to the emission emission sphere, only a small solid angle is detected. The signal flux is determined by the Raman and NV^- scattering cross sections.

3.2.2 Excitation Source

Our excitation source was a Coherent OBIS 532 nm diode laser. Producing a high quality Gaussian beam ($M^2 \leq 1.1$) and spacial (transverse) mode TEM_{00} giving good beam circularity, as shown in table 3.1.

3.2.3 APD Photon Detectors and Imaging Counters

Signal counts were detected by passing the signal from the output fiber into a prearranged Avalanche Photo Diode (APD) coupling setup. To further avoid detector saturation a 650 nm long pass filter was placed prior to the APD aperture. Perkin Elmer, SPCM-AQR-14 APDs were used as photon detectors with peak detection efficiency at 650 nm. The APD has a refresh time resolution of 400 ps and a 50 ns designed dead time between Transistor-Transistor Logic (TTL) pulses. TTL pulses are only generated when specific voltage, current and timing parameters are met, with 5-10 ns pulse widths.

TABLE 3.1: Coherent OBIS 532LS Operational Specifications.

Model	OBIS 532LS
Wavelength	532 nm
Power Range	1-160 mW
Spacial Mode	TEM ₀₀
Beam Quality (M ²)	≤ 1.1
1/e ² Beam Diameter	0.7 ± 0.05
Beam Divergence	≤ 1.2 mRad
Pointing Stability	≤ 5 μ Rad/ $^{\circ}$ C
Noise (20 Hz to 20 kHz)	≤ 0.25 RMS
Polarisation Ratio	100:1, $\pm 5^{\circ}$ Vertical
Long Term Stability (8 hrs)	$\leq 2\%$
Warm Up Time	≤ 5 mins

The APDs were connected to a National Instruments (NI) signal counter box (NI PXIe-1078) with an NI PXIe-6363 X-series signal counter/timer card. TTL pulses generated by the APD were timed and counted by this card which is operated in parallel to an NI PXIe-8360 module control card connected to the Attocube ANSxy50 and ANSz50 continuous scanner stack. This provides simultaneous scan and signal counting capability which along with Qudi laboratory module management suite produces confocal images over an $30\mu\text{m} \times 30\mu\text{m}$ area [84].

3.2.4 Translation, Scanning and Thermal stages

An Attocube piezo stepping translation stack (two ANPx51 and an ANPz51) connected to an Attocube ANC300 piezo controller was employed. While the Attocube scanner stack connected to an Attocube ANC250 10V amplifier was secured on top of the translation stage. The Attocube ANP stages have a weight limit of 25g and with the stack assembled this is reduced to 6.5g. With the resistor heating element weight $\sim 5\text{g}$ and insulation $\sim 3\text{-}5\text{g}$ we exceeded the recommend weight limit however operation was still reliable. With this stage setup we performed the characterization studies given the sub-gram weight of the samples.

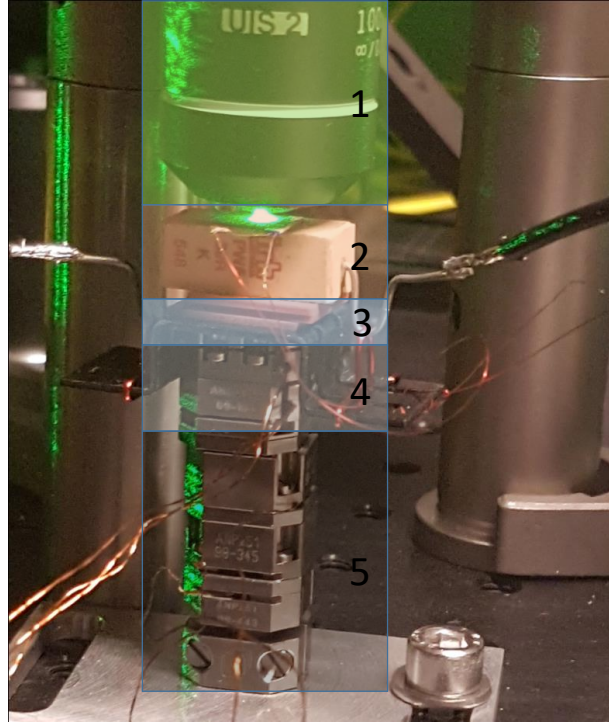


FIGURE 3.3: Image of our Attocube piezo stack. 1. The 100x objective lens, 2. 5 W resistance heating element, 3. Insulating layer of silicon and heat sync, 4. ANSxy50/z50 Attocube continuous scanning stages, 5. ANPz51/x51 Attocube stepping translation stages.

The device sample weight was in excess of the Attocube translation stage weight limit so a thorlabs linear XYZ (MBT613D/M) replaced the ANPx51 and ANPz51 piezo stepping stages. The Attocube scanning stack was glued to an aluminum slab screwed to the linear stage. The device mounted on the heating element was within $\sim 10\text{-}15\text{g}$ of the ANSxy50 and ANSx50 weight limits.

The thermal control element of the stage is a 39Ω , 5W resistor. The resistor was wire bound to the heat sync with silicon insulation in between, shown in figure 3.3.

A platinum resistance thermometer (PT100) was pasted to the surface of the thermal resistor using conductive silver paint. This was used for temperature readout connected to a multimeter. It is designed to be at 100Ω at 0°C and a 0.4Ω increase in resistance corresponds to one degree increase in temperature, with a 20s response time and 0.3° temperature accuracy.

3.2.5 Monochromator

A Princeton Instruments SpectraPro Acton 2500i monochromator was used, with a Pixis 100 CCD Camera (specifications given in table 3.2). The CCD camera has 1340×100 , 20×20 mm pixels with 100% fill factor. Two gratings were mounted on a triple turret a 300 g/mm grating and a 1200 g/mm grating with a 750 nm blazing. Collimated light from the confocal output fiber is focused into the monochromator using a 150mm lens.

Utilising a Raman spectrometer for this application would have been the optimal solution providing the best throughput and resolution. However we did not have the resources available to acquire or borrow a this device, but our current spectrometer provided sufficient counts and resolution for accurate Raman line detection.

TABLE 3.2: Princeton Instruments SpectraPRO Acton 2500i Monochromator Specifications.

Spectrometer Model	Spectra Pro Acton 2500i
Focal Length	500 mm
Aperture Ratio	f/6.5
Scan Range	0-1400 nm
CCD Resolution	0.09 nm
@ 435.8 nm, 20 μ m slit width	
Linear Dispersion	1.52 nm/mm
@ 435.8 nm	
PMT Resolution	0.05 nm
Wavelength Coverage	41 nm
Grating Size	68 \times 68
Wavelength Accuracy	± 0.2 nm
Repeatability	± 0.05 nm

4

Raman Thermometry with Diamond

Here we present the experimental work completed over the course of this project. Results are presented in terms of the first order Raman peak shift and line width broadening for both bulk and nano diamond temperature characterisations. These characterisations provide the basis to determine the Raman temperature for a device measurement. Finally, we demonstrate the goal of this thesis, a device measurement on a GaN FET gate, and discuss the validity and potential of nanodiamond as a high spatial resolution temperature sensor.

4.1 Bulk Diamond Characterisation

In order to demonstrate the capabilities of our confocal system, Raman spectroscopy was performed on a bulk diamond sample. The diamond sample is type IIa with dimensions $2 \times 2 \times 0.5$ mm, and it was implanted in some regions with nitrogen. The dose was low enough

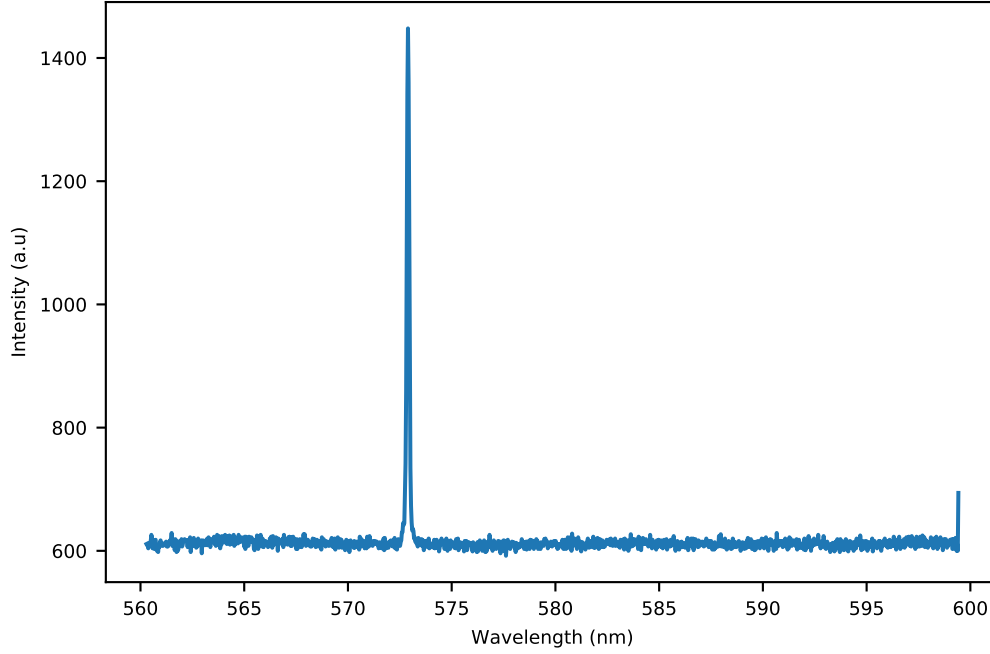


FIGURE 4.1: The first order Raman line of the bulk diamond sample plotted over the complete wavelength of the monochromator with the 1200 g/mm grating.

to produce spatially isolated nitrogen-vacancy centres for previous studies (~ 1 part per billion). The diamond was glued to the resistor heating element on our Attocube scanner and translation stages.

The current to the resistor was increased at 0.01 A increments, which were the smallest allowed by the Dick Smith Q1770 power supply. A total of 252 Raman spectra measurements with 50 current increments up to 0.49 A were performed (5 measurements per increment) over a two day period. An example spectrum is shown in figure 4.1.

These measurements were conducted with the uncoated glass beam sampler confocal setup (instead of the dichroic mirror in figure 3.2). This beam sampler only reflected between 4-5% (0.65 ± 0.005 mW) of the 14.5 ± 0.05 mW input beam for illumination of the diamond. Our return signal beam after the bulk optic had power 0.01 ± 0.005 mW, most of which was laser scatter. All Raman spectra were taken with a 30 second monochromator exposure time using a 1200 g/mm grating. This gives a 40 nm wavelength range (shown in figure 4.1) leaving the 532 nm laser/Rayleigh line just out of detection range.

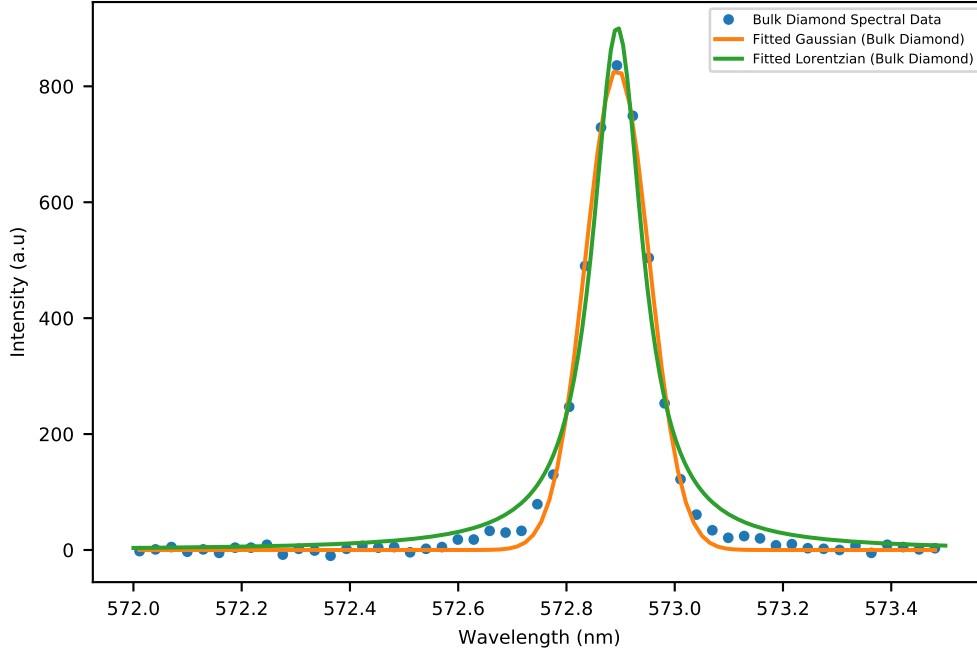


FIGURE 4.2: The first order Raman line of the bulk diamond sample with fitted Gaussian and Lorentzian profiles.

Gaussian and Lorentzian profiles were both fitted to the Raman line as illustrated in figure 4.2, and the peak position and line width were determined from the fits. It is evident in figure 4.2 that the measured Raman spectrum was a closer fit to the Gaussian profile. The expected line shape depends on the factors that limit the spectral resolution.

The OBIS diode laser is unlikely to contribute to the broadening since the laser linewidth is less than MHz, well below the observed linewidths. Since the diamond sample was previously used for single-site nitrogen-vacancy measurements, the concentration of such defects in the diamond sample is too low to cause any broadening. No NV spectra were observed in this study.

Misalignment of the diffraction grating is not significant in this case as the spectrometer was carefully aligned by minimising the point density function on the CCD camera. Slit width was well defined, with the return beam passing through a single mode fiber having a mode field diameter of $\sim 3\text{-}4\ \mu\text{m}$ (an effective pin hole). A 150 mm focal length lens was used to focus the light into the monochromator, producing a light cone that did not fill the grating (a 16 mm

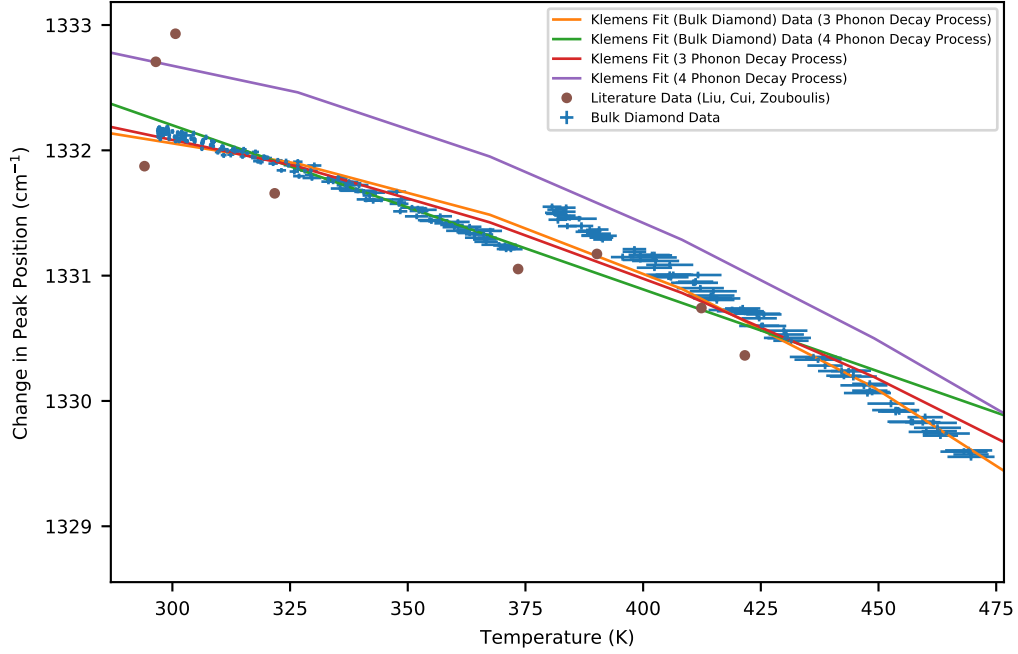


FIGURE 4.3: Temperature dependent Raman peak shift characterisation of the bulk diamond from Gaussian fits. The orange and green curves are the least squares fit of the three phonon and four phonon decay models respectively to the data (blue solid points). The red and purple curves represent the three and four phonon thermal decay models respectively as least squares fits to the digitised literature data (solid brown points) [57, 63, 64].

focal length lens would be required to achieve that for 532 nm light). Underfilling the grating reduces the resolution slightly, although in this case the observed resolution was still close to the expected instrument performance.

It is concluded that the measured width of the Raman line essentially represents the resolution limit of the spectrometer. For this reason a Gaussian profile is used to fit the spectra [85]. This makes it unnecessary to include Raman line characterisations based on Lorentzian fits as peak position would remain the same for both Gaussian and Lorentzian and more accurate line widths can be determined from Gaussian fits.

The three and four phonon decay models fitted to the relative peak shift Data in figure 4.3 and 4.7 are given by equations 2.13 and 2.14 respectively. The three phonon decay model (equation 2.15) is used to fit the Raman linewidth data in figures 4.5 and 4.8.

Figure 4.3 represents the change in Raman peak position relative to an assumed 532nm

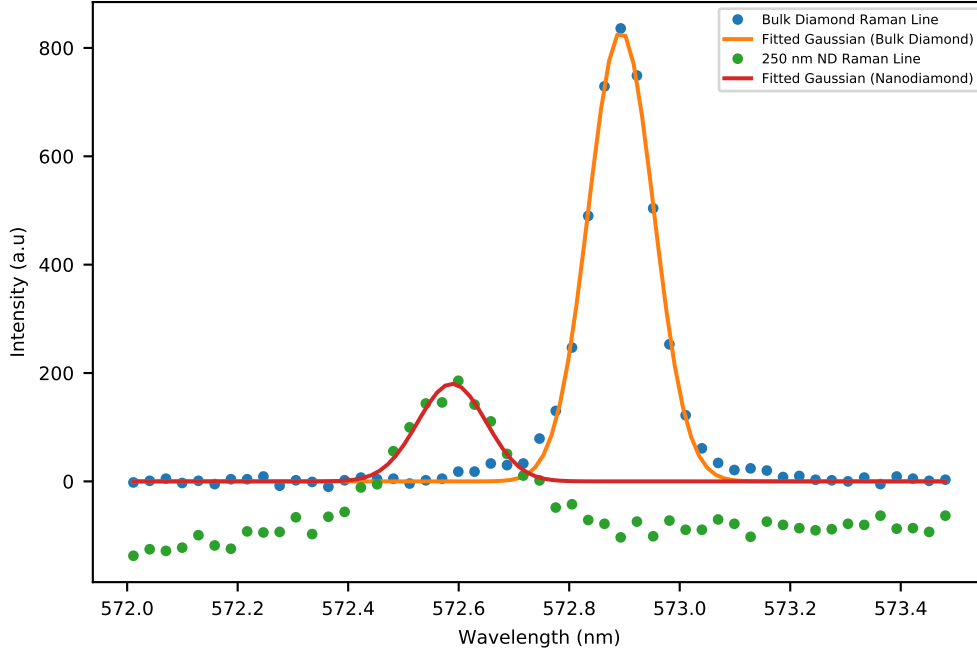


FIGURE 4.4: Gaussian fits to the first order Raman lines of bulk (blue data with orange Gaussian curve) and ND data (green data fitted red Gaussian curve). The position shift is due monochromator realignment.

laser line position. The discontinuity in the data around 375 K was caused by a change in lab temperature conditions from day one to day two, causing possible changes in the laser wavelength (within ± 2 nm tolerance), monochromator alignment in both coupling and grating position and the temperature of the diamond itself.

The temperature resolution is estimated by taking the average fitting error in figure 4.3 and determining its relative temperature change from a chosen reference position value of 1332 cm^{-1} . The temperature error caused by the fitting error was estimated to be 3.8 K. However taking into account the average temperature readout error of 2 K, the Raman peak position temperature characterisation has possible errors between 5-10 K.

The Raman peak is an energy shift from the excitation laser, which was assumed here to be at 532 nm. To achieve better overlap with the literature data, a calibration offset was required. This correction factor was calculated by taking the average difference of the Raman peak positions with there expected position on the three phonon decay curve fitted with digitised

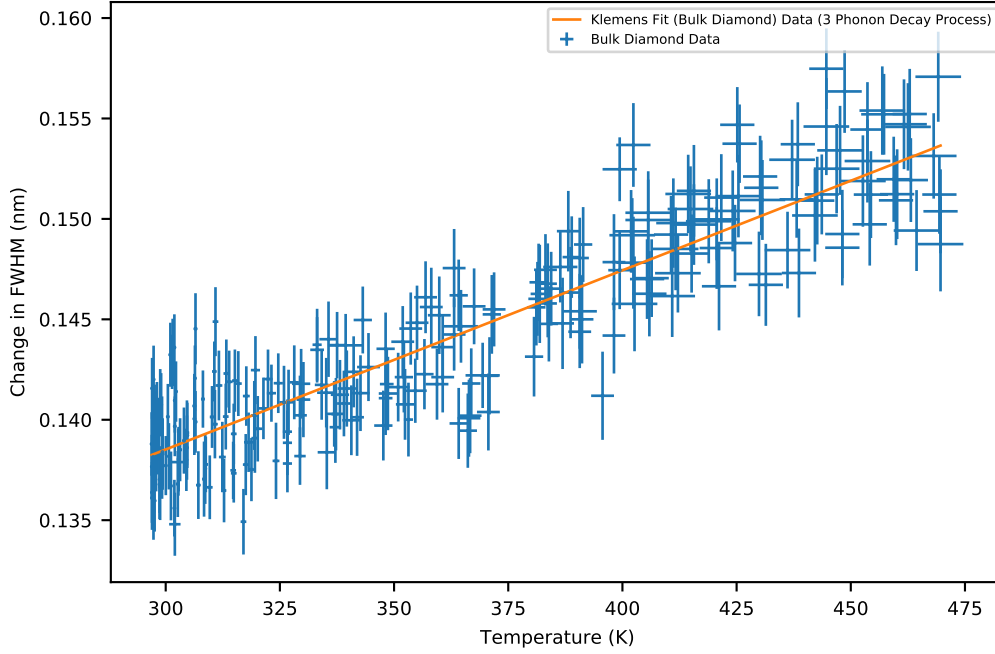


FIGURE 4.5: Temperature dependent characterisation of the Raman width broadening from Gaussian fits for the bulk diamond sample

data from Zouboulis, Cui and Lui [57, 63, 64]. It was hoped to account for the observed ~ 0.35 nm/ 10.5 cm^{-1} offset of the Raman line position from its expected position, shown in figure 4.4. However, an unquantified intrinsic error is induced by this correction factor, which doesn't perfectly account for the spectral offset.

A good understanding of the monochromator resolution is required to accurately characterise and compare the thermal dependence of the Raman line width. Since the actual Raman line width is below the resolution of most monochromators, the measured line widths result from limiting instrument resolution. However, some thermal broadening is still detectable. Lui reviews this in a table showing the evolution of extracted Raman line-widths of different studies over time with good experiment and theory agreement being found for a Raman line width of $1.01 \text{ cm}^{-1}/0.03 \text{ nm}$ (for 532 nm excitation) for temperatures 300 K or less [64, 86]. However, Figure 4.5 shows we did not achieve such accuracies making it difficult to graphically compare to literature data, but we were able to observe a general increase in the line width with increasing temperature.



FIGURE 4.6: Image of the evaporation nanodiamond sample after being removed from the furnace.

It was assumed that the temperature of the diamond was close to that readout by the PT100 thermocouple which was glued to the resistor with a thermally conductive silver paint adhesive. In figure 4.3 and 4.5 the readout error of the thermocouple increased with temperature even after it was left to thermally stabilize for 3-5 minutes. It is possible this was caused by variations of the resistor surface temperature which was exposed to thermally unstable ambient lab conditions.

4.2 Nanodiamond Characterisation

A nanodiamond sample was prepared in order to characterise the Raman spectrum from smaller crystals. We used high grade 250 nm size nanodiamonds that were sorted to within 10-20 nm of the specified size. The nanodiamonds were in distilled water solution with 1 mg/1 cm³ concentration. A small $\sim 1\text{-}3\ \mu\text{L}$ drop on the edge of the container housing the nanodiamonds was selected (containing tens of millions of nanodiamonds) using a 20 μL pipette, and was placed on the center of a glass sample slide which had been wiped clean with acetone. The sample was then placed in a furnace for 15 minutes at 550°C to remove impurities and reduce the evaporation time. The high concentration of nanodiamonds formed a visible ring around the edge of the droplet from its water tension, as shown in figure 4.6. We do not expect nanodiamonds to be outside the droplet ring but it is possible isolated single nanodiamonds exist in the center of the ring.

We experienced difficulty maintaining position on a ND as the Attocube scanner stage would

drift, most likely caused by exceeding the Attocube's operational weight limit. Scanner stage drift was also observed as distortions and diagonal offsets in the confocal image generation, limiting our ability to repeatedly address nanodiamonds positions. In order to measure strong Raman signal from nanodiamonds for this characterisation, the measurement was made on the dense ring. It should be noted the monochromator was realigned before taking these measurements in an attempt to eliminate the offset observed during the bulk diamond investigation. This change in calibration is indicated in figure 4.4

Raman spectra were recorded for illumination power of $6.4 \text{ mW} \pm 0.05 \text{ mW}$. The heating process was repeated as for the bulk diamond sample, with the resistor incremented 50 times up to 0.49 A producing a maximum temperature of $\sim 450 \text{ K}$. Figure 4.7 shows the Raman peak position as a function of temperature. These data are plotted as the Raman shift relative to the assumed 532 nm laser line position. We estimated the temperature resolution of the nanodiamond Raman peak shift to be 22.5 K , which is almost double that obtained for the bulk diamond investigation.

An artifact in the data which is analogous to an oscillation motion is clearly visible. This was caused by a drift of the translation stage with temperature, changing the measurement region to one which is warmer. The position of the confocal microscope was reoptimised eight times during the measurement process, which is observed as the number of troughs and peaks in figure 4.7. These artifacts suppressed the slight curvature required to properly fit the phonon decay models, instead both three and four phonon decay models follow the same effective linear relation (over lapping). In any case the data maps well to the literature data after correcting for possible monochromator offset. Figure 4.7 displays promising but not optimal Raman temperature readout curves over the current temperature range.

Again, the Raman line width was measured as function of temperature, as shown in figure 4.8. The oscillation artifacts are also present, although harder to distinguish with the larger errors.

The errors in both figure 4.7 and 4.8 are caused by Gaussian fits which are not optimal, as shown in figure 4.4. The base line spectral noise is zeroed in both Bulk and ND cases and we have not accounted for the broad Nitrogen vacancy fluorescence, saturating the base of the nanodiamond Raman line. This means our Raman peak widths do not represent the true full

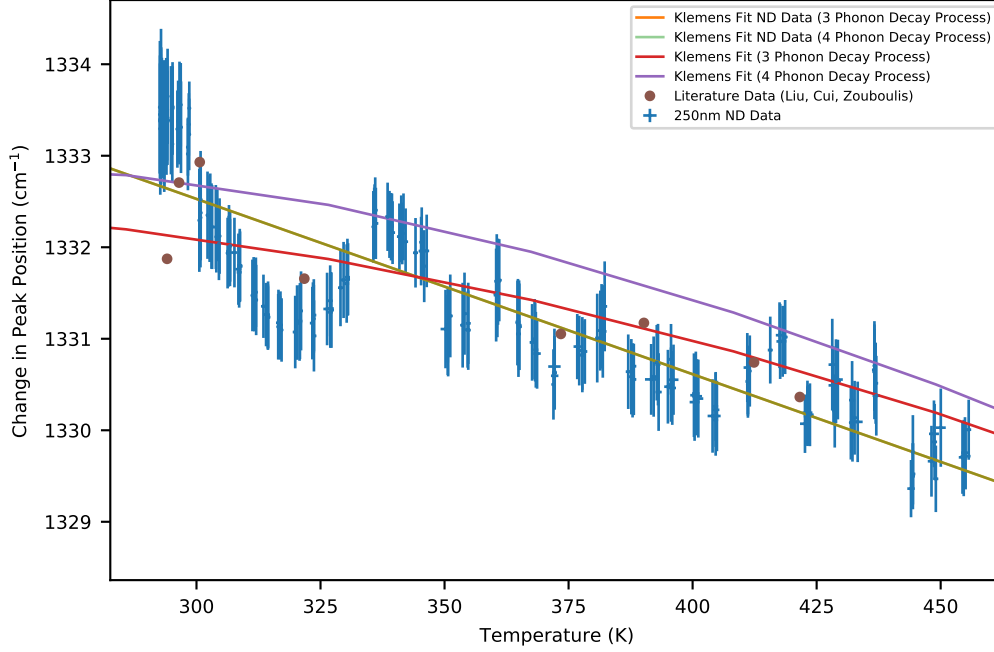


FIGURE 4.7: Temperature dependent Raman peak shift characterisation of the ND evaporation sample from Gaussian fits. The orange and green curves are the least squares fit of the three phonon and four phonon decay models respectively to the data (blue solid points). The red and purple curves represent the three and four phonon thermal decay models respectively as least squares fits to the digitised literature data (solid brown points) [57, 63, 64].

width half maximum of the nanodiamond Raman line. Deconvolution analysis of the Raman would be required to extract the entire Raman line and determine its actual width. This means the results in figure 4.8 do not exhibit the accuracy required to reliably readout the Raman temperature with errors ranging from 20-30% and non-optimal Gaussian fits.

The ambient temperature peak widths are almost identical to those of the bulk diamond line-widths at the same temperature. We interpret this as confirmation of the bulk diamond treatment of the 250 nm NDs, i.e. they are large enough that the phonon confinement effect contributes little if any line-width broadening or frequency shifting of the Raman line [65, 66, 87].

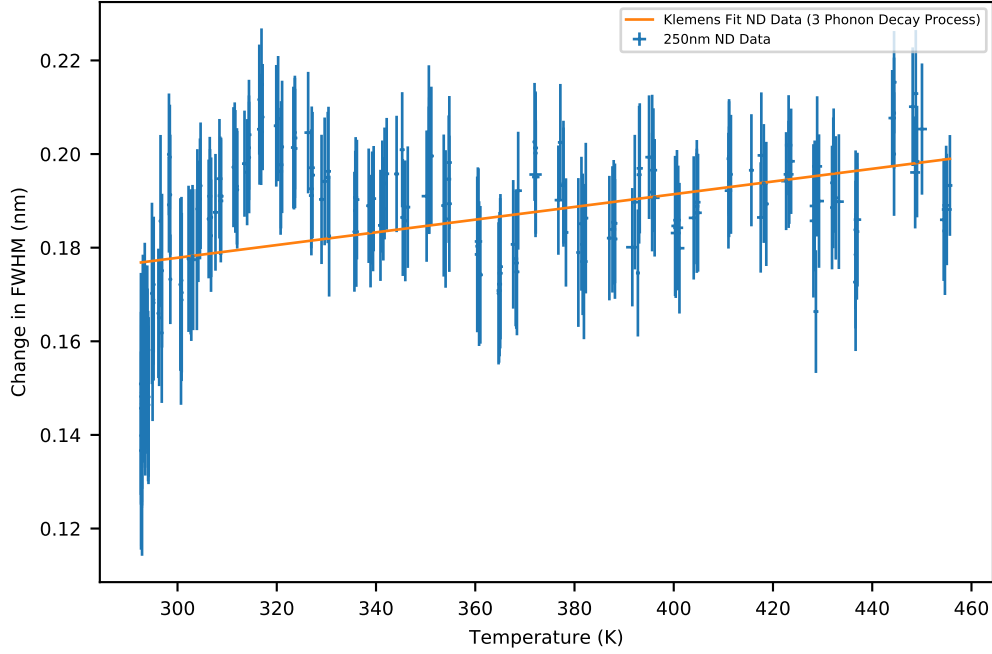


FIGURE 4.8: Temperature dependent characterisation of the Raman width broadening from Gaussian fits for the nanodiamond evaporation sample. The orange line is the least squares fit of the three phonon decay model to the data (blue solid points).

4.3 GaN FET Device Measurement

4.3.1 FET setup and Operation

With a solid understanding of the Raman temperature dependence it is possible to apply Raman thermometry with nanodiamond to an electronic device measurement. Here we are using an eight finger Gallium Nitride (GaN) Field Effect Transistor (FET). The FET is designed with the gate channel open when unbiased (in depletion mode), it requires a positive drain and negative gate voltage relative to a ground source (which limits the drain current) in-order to achieve high drain voltages and channel powers up to a few Watts per gate width.

In this case we applied an open channel condition, allowing high current through put but low voltage. This is a result of the basic power supply available to us at the time. However, we were able to achieve powers up to half a Watt in open channel mode which we expected to produce detectable heating.

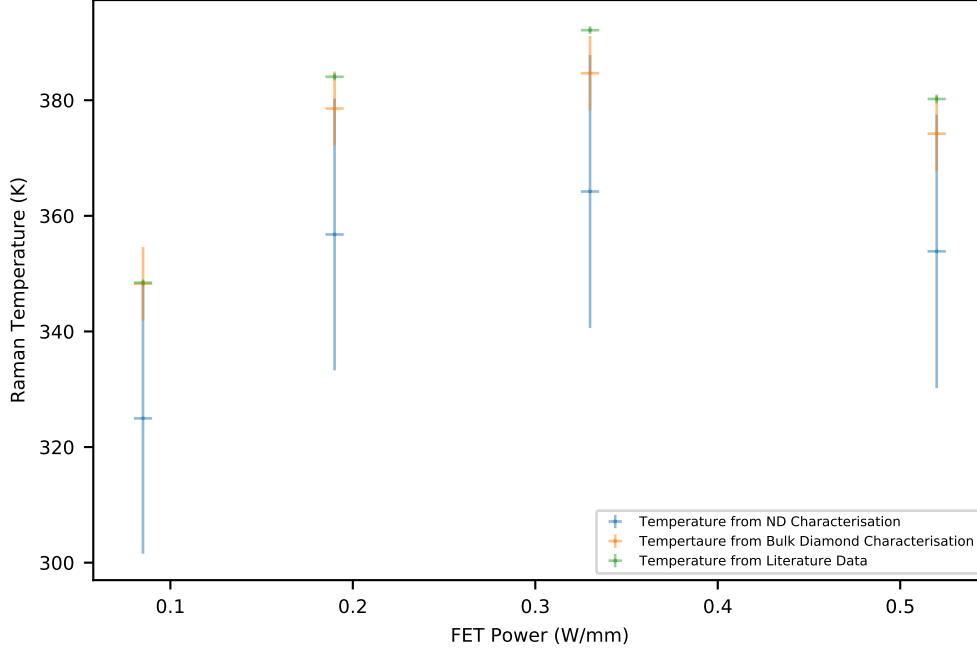


FIGURE 4.9: Raman temperature measurement of 250 nm ND on a GaN FET gate from Gaussian fits. Blue, orange, and green points represent the calibrated Bulk diamond, nanodiamond and literature Raman temperatures.

The size, in particular the width, of the FET governs the amount of power which can be handled. For multi-finger FETs the width is taken as the product of the number of fingers and the width of a single gate. Our FET has 8 fingers and a gate width of $125\ \mu\text{m}$ so the FET width is 1 mm.

The 250 nm nanodiamonds sample was prepared by diluting a small batch of nanodiamonds to a concentration of $0.05\text{mg}/\text{cm}^3$ (hundreds of millions of nanodiamonds). The batch sample was then sonicated for 10-15 minutes to prevent nanodiamonds from clustering. After sonication about $\sim 0.25\ \text{mL}$ of the diluted nanodiamond solution was placed in an micro-AIR Omron nebuliser and sprayed directly onto the GaN device. We calculated one nanodiamond for every 20 drops which are $5\ \mu\text{m}$ in size, from the nebuliser.

The Raman temperatures measured in figure 4.9 were from nanodiamond/s on the gate as shown in the confocal scan in figure 4.10. The FET gate has gold material for the field plate and the source and drain elements, and gold causes broad fluorescence. The nanodiamond Raman

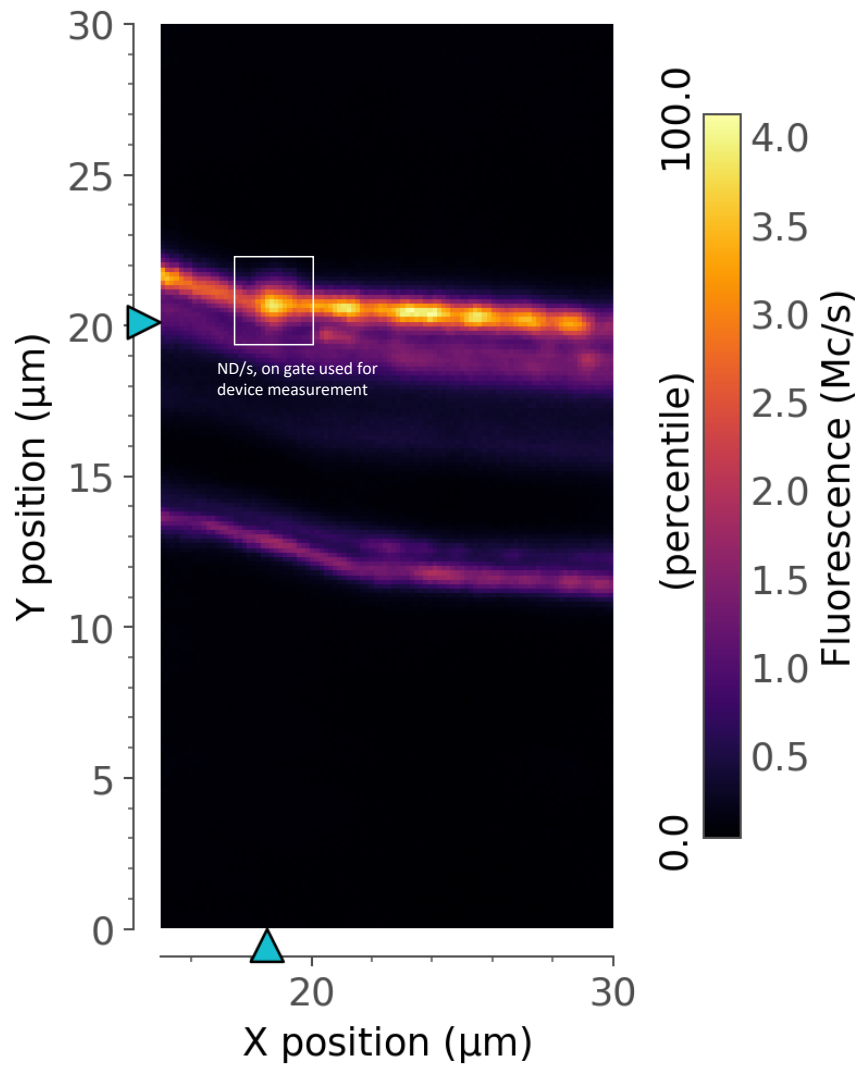


FIGURE 4.10: Confocal scan of one of the 8 finger FET gate regions. Scan was taken over a $15\mu\text{m} \times 30\mu\text{m}$ region.

line was more intense than the gold florescence allowing for peak position extraction. However, deconvolution analysis of the spectrum would be required to extract the Raman line-width, and time limitations have prevented this analysis. This is not a severe limitation, since it has been established above that the peak position provides a more sensitive temperature measurement than linewidth.

Each Raman temperature point is an average of five measurements, allowing the ambient condition fluctuations to be quantified and included in the error. These were found to be insignificant. The calibration data errors were averaged for peak shift, and in each case an estimated error was determined. The average temperature readout error for the calibration curves was also considered. The ND calibration curve errors for bulk diamond and nanodiamond were particularly significant $\sim \pm 25$ degrees. The horizontal error is systematic to the power supply which only displayed current and voltages to two decimal values.

The errors quantified in figure 4.9 do not account for all possible uncertainties. As previously discussed, the relative Raman peak position to the Rayleigh scattering line wasn't directly calculated due to limited (40 nm) spectral range. Again, there is an intrinsic uncertainty that comes with our assumption that the Rayleigh line is centered at 532 nm. Even through we attempt to correct for this uncertainty using known aligned literature data, this uncertainty carries through to our device measurement.

We expect the temperature power relation on the gate to be non-linear given the dependence of thermal conductivity of GaN is non-linear [28]. Over small temperature range we can assume an approximately linear change in thermal conductivity for both GaN and gold [28, 88]. We observe a large Raman temperature increase between 0.085 W/mm and 0.19 W/mm, ~ 15 degrees, possibly within our detection resolution of 5-15 K for bulk diamond calibration. The Raman temperature seems to reach a saturation point after 0.19 W, the cause of which is unknown. However, it is possible that the Raman temperature readouts after 0.19 W/mm are actually temperature changes below our detection resolution, meaning they appear as noise. This would account for the drop in temperature at 0.52 W/mm. If what we extracted was representative of temperature (unlikely option) then further investigation is necessary. Either way it would be interesting to see further investigations to discern with certainty what we are detecting and extracting is representative of the actual temperature of the nanodiamond.

5

Outlook

The experimental results presented in this thesis are a first step towards the implementation of a robust nanoscale thermometer based on Raman scattering from nanodiamonds. The initial characterisation of diamond samples has been successful, and a preliminary application of this technique to industrially-relevant devices has been shown. While the results as such look promising and warrant further pursuit of this interesting research direction, there is still considerable work to do before true nanoscale temperature read-out can be claimed.

Unfortunately, thermometry on a single nanodiamond with subdiffraction limited spatial resolution could not be demonstrated in this work due to technical limitations of the basic confocal setup and the shortage of effective lab time. The most severe limitation in this regard was the Attocube scanner used for confocal microscope imaging, which was unable to provide the stability and repeatability required to locate and track an isolated ND throughout the temperature measurement. The lab is equipped with a more capable AFM/confocal platform,

but this was unavailable for the duration of this project due to an unexpectedly prolonged rebuilding operation. When it is operational again the measurements on single nanodiamonds should be easily within reach.

Once single nanodiamond Raman scattering is well-established, one can push for smaller sizes of ideally 100-150 nm, a length scale that is technically relevant due to the typical widths of wires on semiconductor chips. It would also be beneficial to improve the capabilities of the spectrometer. Given that the Raman signal scales with the volume of the nanodiamond, every photon counts and so improved collection efficiency would increase the measurement speed. The Quantum Materials and Applications (QMAPP) group at Macquarie University is collaborating with a colleague in Astrophotonics who is a world-expert in building astro-spectrographs. He and his group have developed an advanced spectrometer that would be ideally suited for diamond Raman spectroscopy. This instrument has an anticipated improvement in both resolution and throughput by at least a factor of two compared to the currently used system, and the ability to record spectra over several hundred nanometers with high resolution. As well as improving the signal-to-noise ratio, these features would allow for reading out the position of Stokes/Anti-Stokes and Rayleigh line in a single exposure, enabling an accurate readout of relative peak positions.

Before nanodiamonds can be used for nanoscale temperature read-out in a robust and routine fashion, more research steps are needed. Different nanodiamonds of very similar size need to be characterised and their Raman signals compared. A 'universal' nanodiamond Raman thermometer can be realized only if it can be experimentally proven that nanodiamonds of the same size all show essentially the same temperature variation of their Raman signals. Questions of thermal contact and thermal conductivity between substrate and nanodiamond would clearly play a role here. Such investigations will also touch upon more fundamental questions of heat transport and the very definition of temperature at the nanoscale. In fact, having a suitable nanoscale thermometer at hand could allow for the exploration of a whole new range of physics questions connected to heat transport and thermodynamics at the nanoscale. The work presented here has opened the door to these fascinating questions only by a small gap. The students following up in this project will hopefully be able to push the door right open and fully enter into this fascinating area of research.

References

- [1] R. B. Simon, J. W. Pomeroy, and M. Kuball. *Diamond micro-Raman thermometers for accurate gate temperature measurements*. Applied Physics Letters **104**(21), 213503 (2014). URL <http://aip.scitation.org/doi/abs/10.1063/1.4879849>.
- [2] E. Neu, C. Hepp, M. Hauschild, S. Gsell, M. Fischer, H. Sternschulte, Doris Steinmüller-Nethl, M. Schreck, and C. Becher. *Low-temperature investigations of single silicon vacancy colour centres in diamond*. New Journal of Physics **15**(4), 043005 (2013). URL <http://stacks.iop.org/1367-2630/15/i=4/a=043005>.
- [3] P. Vandenabeele. *Raman spectroscopy in art and archaeology*. Journal of Raman spectroscopy **35**(8-9), 607 (2004).
- [4] R. L. McCreery. *Raman spectroscopy for chemical analysis*, vol. 225 (John Wiley & Sons, 2005).
- [5] D. Graf, F. Molitor, K. Ensslin, C. Stampfer, A. Jungen, C. Hierold, and L. Wirtz. *Spatially resolved raman spectroscopy of single-and few-layer graphene*. Nano letters **7**(2), 238 (2007).
- [6] Z. Movasaghi, S. Rehman, and D. I. U. Rehman. *Raman Spectroscopy of Biological Tissues*. Applied Spectroscopy Reviews **42**(5), 493 (2007). URL <http://dx.doi.org/10.1080/05704920701551530>.
- [7] G. Kucsko, P. Maurer, N. Y. Yao, M. Kubo, H. Noh, P. Lo, H. Park, and M. D. Lukin. *Nanometer scale thermometry in a living cell*. Nature **500**(7460), 54 (2013).
- [8] J. Taylor, P. Cappellaro, L. Childress, L. Jiang, D. Budker, P. Hemmer, A. Yacoby, R. Walsworth, and M. Lukin. *High-sensitivity diamond magnetometer with nanoscale resolution*. arXiv preprint arXiv:0805.1367 (2008).
- [9] J. Wrachtrup and F. Jelezko. *Processing quantum information in diamond*. Journal of Physics: Condensed Matter **18**(21), S807 (2006).
- [10] C. V. Raman and K. S. Krishnan. *A new type of secondary radiation*. Nature **121**(3048), 501 (1928).
- [11] R. Loudon. *The Raman effect in crystals*. Advances in Physics **13**(52), 423 (1964). URL <http://dx.doi.org/10.1080/00018736400101051>.
- [12] M. Lax and E. Burstein. *Infrared Lattice Absorption in Ionic and*

- Homopolar Crystals*. Physical Review **97**(1), 39 (1955). URL <https://link.aps.org/doi/10.1103/PhysRev.97.39>.
- [13] S. Lee and E. J. Heller. *Timedependent theory of Raman scattering*. The Journal of Chemical Physics **71**(12), 4777 (1979). URL <http://aip.scitation.org/doi/abs/10.1063/1.438316>.
- [14] D. L. Andrews and A. A. Demidov. *An Introduction to Laser Spectroscopy: Second Edition* (Springer Science & Business Media, 2012). Google-Books-ID: NSvnBwAAQBAJ.
- [15] M. D. Williams, D. S. Bradshaw, and D. L. Andrews. *Raman scattering mediated by neighboring molecules*. The Journal of Chemical Physics **144**(17), 174304 (2016). URL <http://aip.scitation.org/doi/full/10.1063/1.4948366>.
- [16] W. K. Briskel and G. Black. *Wavelength dependence of raman scattering cross sections from 200600 nm*. AIP Conference Proceedings **100**(1), 181 (1983). URL <http://aip.scitation.org/doi/abs/10.1063/1.34046>.
- [17] R. Mildren and J. Rabeau. *Optical Engineering of Diamond* (Wiley, 2013). URL <https://books.google.com.au/books?id=bUB5Dh4m6E4C>.
- [18] J. G. Skinner and W. G. Nilsen. *Absolute Raman Scattering Cross-Section Measurement of the 992 cm⁻¹ Line of Benzene**. JOSA **58**(1), 113 (1968). URL <https://www.osapublishing.org/abstract.cfm?uri=josa-58-1-113>.
- [19] M. Grimsditch, M. Cardona, J. M. Calleja, and F. Meseguer. *Resonance in the Raman scattering of CaF₂, SrF₂, BaF₂ and diamond*. Journal of Raman Spectroscopy **10**(1), 77 (1981). URL <http://onlinelibrary.wiley.com/doi/10.1002/jrs.1250100113/abstract>.
- [20] G. Peschel. *Carbon-carbon bonds: hybridization*. Obtained online from: http://www.physik.fu-berlin.de/einrichtungen/ag/ag-reich/lehre/Archiv/ss2011/docs/Gina_Peschel-Handout.pdf, published on 5(5) (2011).
- [21] C. Kittel. *Introduction to solid state physics* (Wiley, 1976). URL <https://books.google.com.au/books?id=0wJRAAAAMAAJ>.
- [22] C. Bradac *et al.* *The properties of nitrogen-vacancy centres in nanodiamond* (2012).
- [23] C. D. Clark, P. J. Dean, and P. V. Harris. *Intrinsic Edge Absorption in Diamond*. Proceedings of the Royal Society of London A: Mathematical, Physical and Engineering Sciences **277**(1370), 312 (1964). URL <http://rspa.royalsocietypublishing.org/content/277/1370/312>.
- [24] N. Ashcroft and N. Mermin. *Solid state physics*. cengage learning. Inc., New York (1976).
- [25] D. Gaskill, C. D. Brandt, and R. J. Nemanich. *Iii-nitride, sic and diamond materials for electronic devices. symposium held april 8-12 1996, san francisco, california, usa volume*

423. Tech. rep., MATERIALS RESEARCH SOCIETY PITTSBURGH PA (1996).
- [26] C. J. H. Wort and R. S. Balmer. *Diamond as an electronic material*. *Materials Today* **11**(1), 22 (2008). URL <http://www.sciencedirect.com/science/article/pii/S1369702107703498>.
- [27] S. V. Kidalov and F. M. Shakhov. *Thermal Conductivity of Diamond Composites*. *Materials* **2**(4), 2467 (2009). URL <http://www.mdpi.com/1996-1944/2/4/2467>.
- [28] E. Sichel and J. Pankove. *Thermal conductivity of gan, 25–360 k*. *Journal of physics and chemistry of solids* **38**(3), 330 (1977).
- [29] J. E. Field. *The properties of diamond* (Academic Press, 1979).
- [30] G. A. Slack and S. F. Bartram. *Thermal expansion of some diamondlike crystals*. *Journal of Applied Physics* **46**(1), 89 (1975). URL <http://aip.scitation.org/doi/abs/10.1063/1.321373>.
- [31] S. Stoupin and Y. V. Shvydko. *Ultraprecise studies of the thermal expansion coefficient of diamond using backscattering x-ray diffraction*. *Physical Review B* **83**(10), 104102 (2011). URL <https://link.aps.org/doi/10.1103/PhysRevB.83.104102>.
- [32] H. Watanabe, N. Yamada, and M. Okaji. *Linear Thermal Expansion Coefficient of Silicon from 293 to 1000 K*. *International Journal of Thermophysics* **25**(1), 221 (2004). URL <https://link.springer.com/article/10.1023/B:IJOT.0000022336.83719.43>.
- [33] M. Leszczynski, T. Suski, H. Teisseyre, P. Perlin, I. Grzegory, J. Jun, S. Porowski, and T. D. Moustakas. *Thermal expansion of gallium nitride*. *Journal of Applied Physics* **76**(8), 4909 (1994). URL <http://aip.scitation.org/doi/abs/10.1063/1.357273>.
- [34] F. P. Bundy. *Pressure-temperature phase diagram of elemental carbon*. *Physica A: Statistical Mechanics and its Applications* **156**(1), 169 (1989). URL <http://www.sciencedirect.com/science/article/pii/0378437189901155>.
- [35] G. A. Slack. *Effect of Isotopes on Low-Temperature Thermal Conductivity*. *Physical Review* **105**(3), 829 (1957). URL <https://link.aps.org/doi/10.1103/PhysRev.105.829>.
- [36] O. P. Gupta. *Phonon frequencies and Debye temperature of copper*. *Journal of Physics F: Metal Physics* **14**(12), 2899 (1984). URL <http://stacks.iop.org/0305-4608/14/i=12/a=012>.
- [37] C. Roder, S. Einfeldt, S. Figge, and D. Hommel. *Temperature dependence of the thermal expansion of GaN*. *Physical Review B* **72**(8), 085218 (2005). URL <https://link.aps.org/doi/10.1103/PhysRevB.72.085218>.
- [38] M. Seal. *Thin film diamond - Thermal and optical applications of thin film diamond*. *Phil. Trans. R. Soc. Lond. A* **342**(1664), 313 (1993). URL <http://rsta.royalsocietypublishing.org/content/342/1664/313>.

-
- [39] G. E. Harlow. *The nature of diamonds* (Cambridge University Press, 1998).
- [40] D. F. Edwards and E. Ochoa. *Infrared refractive index of diamond*. JOSA **71**(5), 607 (1981). URL <https://www.osapublishing.org/abstract.cfm?uri=josa-71-5-607>.
- [41] A. Zaitsev. *Optical Properties of Diamond: A Data Handbook* (Springer, 2001). URL <https://books.google.com.au/books?id=msU4jkdCEhIC>.
- [42] Y. Mita. *Change of absorption spectra in type-Ib diamond with heavy neutron irradiation*. Physical Review B **53**(17), 11360 (1996). URL <https://link.aps.org/doi/10.1103/PhysRevB.53.11360>.
- [43] R. Robertson and J. Fox. *Infra-red spectrum of diamond by infra-red spectrometer and raman methods*. Nature **125**(3158), 704 (1930).
- [44] C. Ramaswamy. *The raman effect in diamond* (1930).
- [45] S. Bhagavantam. *Further studies on the raman spectrum of diamond*. (1930).
- [46] R. Robertson, J. Fox, and A. Martin. *Two types of diamond*. Philosophical Transactions of the Royal Society of London. Series A, Containing Papers of a Mathematical or Physical Character **232**, 463 (1934).
- [47] N. S. N. Nath. *The dynamical theory of the diamond lattice. I*. Proceedings of the Indian Academy of Sciences - Section A **1**(5), 333 (1934). URL <https://link.springer.com/article/10.1007/BF03035575>.
- [48] S. Bhagavantam and T. Venkatarayudu. *Raman effect in relation to crystal structure*. Proceedings of the Indian Academy of Sciences - Section A **9**(3), 224 (1939). URL <https://link.springer.com/article/10.1007/BF03046465>.
- [49] C. V. Raman. *The Structure and Properties of Diamond*. Current Science **12**(1), 33 (1943). URL <http://www.jstor.org/stable/24208172>.
- [50] H. M. J. Smith. *The Theory of the Vibrations and the Raman Spectrum of the Diamond Lattice*. Philosophical Transactions of the Royal Society of London. Series A, Mathematical and Physical Sciences **241**(829), 105 (1948). URL <http://www.jstor.org/stable/91478>.
- [51] D. Krishnamurti. *The Raman spectrum of diamond*. Proceedings of the Indian Academy of Sciences - Section A **40**(5), 211 (1954). URL <https://link.springer.com/article/10.1007/BF03047399>.
- [52] P. G. Klemens. *Anharmonic Attenuation of Localized Lattice Vibrations*. Physical Review **122**(2), 443 (1961). URL <https://link.aps.org/doi/10.1103/PhysRev.122.443>.
- [53] P. G. Klemens. *Anharmonic Decay of Optical Phonons*. Physical Review **148**(2), 845 (1966). URL <https://link.aps.org/doi/10.1103/PhysRev.148.845>.

- [54] J. Menendez and M. Cardona. *Temperature dependence of the first-order Raman scattering by phonons in Si, Ge, and α - Si_3N_4 : Anharmonic effects*. Physical Review B **29**(4), 2051 (1984). URL <https://link.aps.org/doi/10.1103/PhysRevB.29.2051>.
- [55] R. Cowley. *Raman scattering from crystals of the diamond structure*. Journal de Physique **26**(11), 659 (1965).
- [56] M. Balkanski, R. F. Wallis, and E. Haro. *Anharmonic effects in light scattering due to optical phonons in silicon*. Physical Review B **28**(4), 1928 (1983). URL <https://link.aps.org/doi/10.1103/PhysRevB.28.1928>.
- [57] J. B. Cui, K. Amtmann, J. Ristein, and L. Ley. *Noncontact temperature measurements of diamond by Raman scattering spectroscopy*. Journal of Applied Physics **83**(12), 7929 (1998). URL <http://aip.scitation.org/doi/abs/10.1063/1.367972>.
- [58] R. Krishnan and P. Narayanan. *Intensity ratio of the raman lines in diamond*. In *Proceedings of the Indian Academy of Sciences-Section A*, vol. 32, p. 352 (Springer India, 1950).
- [59] H. Herchen and M. A. Cappelli. *First-order Raman spectrum of diamond at high temperatures*. Physical Review B **43**(14), 11740 (1991). URL <https://link.aps.org/doi/10.1103/PhysRevB.43.11740>.
- [60] R. S. Krishnan. *Temperature variations of the Raman frequencies in diamond*. Proceedings of the Indian Academy of Sciences - Section A **24**(1), 45 (1946). URL <https://link.springer.com/article/10.1007/BF03170739>.
- [61] W. J. Borer, S. S. Mitra, and K. V. Namjoshi. *Line shape and temperature dependence of the first order Raman spectrum of diamond*. Solid State Communications **9**(16), 1377 (1971). URL <http://www.sciencedirect.com/science/article/pii/0038109871903991>.
- [62] E. Anastassakis, H. C. Hwang, and C. H. Perry. *Temperature Dependence of the Long-Wavelength Optical Phonons in Diamond*. Physical Review B **4**(8), 2493 (1971). URL <https://link.aps.org/doi/10.1103/PhysRevB.4.2493>.
- [63] E. S. Zouboulis and M. Grimsditch. *Raman scattering in diamond up to 1900 K*. Physical Review B **43**(15), 12490 (1991). URL <https://link.aps.org/doi/10.1103/PhysRevB.43.12490>.
- [64] M. S. Liu, L. A. Bursill, S. Prawer, and R. Beserman. *Temperature dependence of the first-order Raman phonon line of diamond*. Physical Review B **61**(5), 3391 (2000). URL <https://link.aps.org/doi/10.1103/PhysRevB.61.3391>.
- [65] A. K. Arora, M. Rajalakshmi, T. R. Ravindran, and V. Sivasubramanian. *Raman spectroscopy of optical phonon confinement in nanostructured materials*. Journal of Raman Spectroscopy **38**(6), 604 (2007). URL

- <http://onlinelibrary.wiley.com/doi/10.1002/jrs.1684/abstract>.
- [66] S. Osswald, V. N. Mochalin, M. Havel, G. Yushin, and Y. Gogotsi. *Phonon confinement effects in the Raman spectrum of nanodiamond*. Physical Review B **80**(7), 075419 (2009). URL <https://link.aps.org/doi/10.1103/PhysRevB.80.075419>.
 - [67] H. Richter, Z. P. Wang, and L. Ley. *The one phonon Raman spectrum in microcrystalline silicon*. Solid State Communications **39**(5), 625 (1981). URL <http://www.sciencedirect.com/science/article/pii/0038109881903379>.
 - [68] V. M. Acosta, E. Bauch, M. P. Ledbetter, A. Waxman, L.-S. Bouchard, and D. Budker. *Temperature Dependence of the Nitrogen-Vacancy Magnetic Resonance in Diamond*. Physical Review Letters **104**(7), 070801 (2010). URL <https://link.aps.org/doi/10.1103/PhysRevLett.104.070801>.
 - [69] D. M. Toyli, D. J. Christle, A. Alkauskas, B. B. Buckley, C. G. Van de Walle, and D. D. Awschalom. *Measurement and Control of Single Nitrogen-Vacancy Center Spins above 600 K*. Physical Review X **2**(3), 031001 (2012). URL <https://link.aps.org/doi/10.1103/PhysRevX.2.031001>.
 - [70] J. Wang, F. Feng, J. Zhang, J. Chen, Z. Zheng, L. Guo, W. Zhang, X. Song, G. Guo, L. Fan, C. Zou, L. Lou, W. Zhu, and G. Wang. *High-Sensitivity Temperature Sensing Using an Implanted Single Nitrogen-Vacancy Center Array in Diamond*. Physical Review B **91**(15) (2015). ArXiv: 1410.6893, URL <http://arxiv.org/abs/1410.6893>.
 - [71] D. M. Toyli, C. F. d. l. Casas, D. J. Christle, V. V. Dobrovitski, and D. D. Awschalom. *Fluorescence thermometry enhanced by the quantum coherence of single spins in diamond*. Proceedings of the National Academy of Sciences **110**(21), 8417 (2013). URL <http://www.pnas.org/content/110/21/8417>.
 - [72] P. Neumann, I. Jakobi, F. Dolde, C. Burk, R. Reuter, G. Waldherr, J. Honert, T. Wolf, A. Brunner, J. H. Shim, D. Suter, H. Sumiya, J. Isoya, and J. Wrachtrup. *High-Precision Nanoscale Temperature Sensing Using Single Defects in Diamond*. Nano Letters **13**(6), 2738 (2013). URL <http://dx.doi.org/10.1021/nl401216y>.
 - [73] L. J. Rogers, K. D. Jahnke, T. Teraji, L. Marseglia, C. Mller, B. Naydenov, H. Schauffert, C. Kranz, J. Isoya, L. P. McGuinness, and F. Jelezko. *Multiple intrinsically identical single-photon emitters in the solid state*. Nature Communications **5**, ncomms5739 (2014). URL <https://www.nature.com/articles/ncomms5739>.
 - [74] A. Sipahigil, K. Jahnke, L. Rogers, T. Teraji, J. Isoya, A. Zibrov, F. Jelezko, and M. Lukin. *Indistinguishable Photons from Separated Silicon-Vacancy Centers in Diamond*. Physical Review Letters **113**(11), 113602 (2014). URL <https://link.aps.org/doi/10.1103/PhysRevLett.113.113602>.
 - [75] L. J. Rogers, K. D. Jahnke, M. W. Doherty, A. Dietrich, L. P. McGuinness, C. Müller, T. Teraji, H. Sumiya, J. Isoya, N. B. Manson, *et al.* *Electronic structure of the negatively*

- charged silicon-vacancy center in diamond*. Physical Review B **89**(23), 235101 (2014).
- [76] J. N. Becker, B. Pingault, D. Gro, M. Gndoan, N. Kukharchyk, M. Markham, A. Edmonds, M. Atatré, P. Bushev, and C. Becher. *All-optical control of the silicon-vacancy spin in diamond at millikelvin temperatures*. arXiv:1708.08263 [cond-mat, physics:quant-ph] (2017). ArXiv: 1708.08263, URL <http://arxiv.org/abs/1708.08263>.
- [77] K. Dragounov, Z. Potek, . Potock, Z. Bryknar, and A. Kromka. *Determination of temperature dependent parameters of zero-phonon line in photo-luminescence spectrum of silicon-vacancy centre in CVD diamond thin films*. Journal of Electrical Engineering **68**(1), 74 (2017). URL <https://www.degruyter.com/view/j/jee.2017.68.issue-1/jee-2017-0010/jee-2017-0010.xml>
- [78] S. Lagomarsino, F. Gorelli, M. Santoro, N. Fabbri, A. Hajeb, S. Sciortino, L. Palla, C. Czelusniak, M. Massi, F. Taccetti, L. Giuntini, N. Gelli, D. Y. Fedyanin, F. S. Cataliotti, C. Toninelli, and M. Agio. *Robust luminescence of the silicon-vacancy center in diamond at high temperatures*. AIP Advances **5**(12), 127117 (2015). URL <http://aip.scitation.org/doi/full/10.1063/1.4938256>.
- [79] K. D. Jahnke, A. Sipahigil, J. M. Binder, M. W. Doherty, M. Metsch, L. J. Rogers, N. B. Manson, M. D. Lukin, and F. Jelezko. *Electronphonon processes of the silicon-vacancy centre in diamond*. New Journal of Physics **17**(4), 043011 (2015). URL <http://stacks.iop.org/1367-2630/17/i=4/a=043011>.
- [80] G. J. Riedel, J. W. Pomeroy, K. P. Hilton, J. O. Maclean, D. J. Wallis, M. J. Uren, T. Martin, and M. Kuball. *Nanosecond Timescale Thermal Dynamics of AlGaIn/GaN Electronic Devices*. IEEE Electron Device Letters **29**(5), 416 (2008).
- [81] A. Sarua, H. Ji, M. Kuball, M. J. Uren, T. Martin, K. P. Hilton, and R. S. Balmer. *Integrated micro-Raman/infrared thermography probe for monitoring of self-heating in Al-GaN/GaN transistor structures*. IEEE Transactions on Electron Devices **53**(10), 2438 (2006).
- [82] C. Sheppard and D. Shotton. *Confocal Laser Scanning Microscopy*. Microscopy handbooks (BIOS Scientific, 1997). URL <https://books.google.com.au/books?id=MCuoGu7t2Q4C>.
- [83] M. Minsky. *Memoir on inventing the confocal scanning microscope*. Scanning **10**(4), 128 (1988).
- [84] J. M. Binder, A. Stark, N. Tomek, J. Scheuer, F. Frank, K. D. Jahnke, C. Mller, S. Schmitt, M. H. Metsch, T. Uden, T. Gehring, A. Huck, U. L. Andersen, L. J. Rogers, and F. Jelezko. *Qudi: A modular python suite for experiment control and data processing*. SoftwareX **6**, 85 (2017). URL <http://www.sciencedirect.com/science/article/pii/S2352711017300055>.
- [85] K. Michaelian and W. Friesen. *Deconvolution of instrumental broadening in dispersive raman spectroscopy*. Applied Spectroscopy **42**(8), 1538 (1988).

-
- [86] A. Debernardi, S. Baroni, and E. Molinari. *Anharmonic Phonon Lifetimes in Semiconductors from Density-Functional Perturbation Theory*. Physical Review Letters **75**(9), 1819 (1995). URL <https://link.aps.org/doi/10.1103/PhysRevLett.75.1819>.
 - [87] K. Sun, J. Y. Wang, and T. Y. Ko. *Raman spectroscopy of single nanodiamond: Phonon-confinement effects*. Applied Physics Letters **92**(15), 153115 (2008). URL <http://aip.scitation.org/doi/abs/10.1063/1.2912029>.
 - [88] M. T. Carlson, A. J. Green, A. Khan, and H. Richardson. *Optical measurement of thermal conductivity and absorption cross-section of gold nanowires* **116**, 8798 (2012).